1985

# Structure of transitionally rough and fully rough turbulent boundary layers

Ligrani, Phillip M.; Moffat, Robert J.

Cambridge University Press

Ligrani, Phillip M., and Robert J. Moffat. "Structure of transitionally rough and fully rough turbulent boundary layers." Journal of Fluid Mechanics 162 (1986): 69-98.
http://hdl.handle.net/10945/62207

*J. Fluid Mech.* (1986), *vol.* 162, *pp.* 69–98
*Printed in Great Britain*



# Structure of transitionally rough and fully rough turbulent boundary layers

By PHILLIP M. LIGRANI
Department of Mechanical Engineering, Naval Postgraduate School, Monterey, CA 93943

AND ROBERT J. MOFFAT
Department of Mechanical Engineering, Thermosciences Division, Stanford University, Stanford, California 94305

(Received 21 May 1984 and in revised form 20 June 1985)

Structural characteristics of transitionally rough and fully rough turbulent boundary layers are presented. These were measured in flows at different roughness Reynolds numbers developing over uniform spheres roughness. Inner regions of the longitudinal component of normal Reynolds stress profiles and log regions of mean profiles continuously change in the transitionally rough regime, as the roughness Reynolds number, $Re_k$, varies. These properties asymptotically approach fully rough behaviour as $Re_k$ increases, and smooth behaviour at low $Re_k$. Profiles of other Reynolds-stress tensor components, turbulence kinetic energy, turbulence-kinetic-energy production, and the turbulence-kinetic-energy dissipation are also given, along with appropriate scaling variables. Fully rough, one-dimensional spectra of longitudinal velocity fluctuations from boundary-layer inner regions are similar to smooth-wall results for $k_1 y > 0.2$ when non-dimensionalized using distance from the wall $y$ as the lengthscale, and $(\tau/\rho)^{\frac{1}{2}}$ as the velocity scale, where $\tau$ is local shear stress, $\rho$ is static density, and $k_1$ is one-dimensional wavenumber in the flow direction.

## 1. Introduction

Transitionally rough turbulent boundary layers exist for the range of roughness Reynolds numbers between smooth and fully rough flow regimes. The roughness Reynolds number, $Re_k$, is defined as the ratio of the equivalent sandgrain roughness height, $k_s$, to viscous length, $\nu/U_\tau$. $Re_k$ may also be viewed as the non-dimensional sandgrain roughness height in $y^+$ coordinates, where $y^+ = yU_\tau/\nu$, with $U_\tau$ equal to the friction velocity, $y$ the normal distance from the wall, and $\nu$ the kinematic viscosity. Consequently, the magnitude of $Re_k$ may be compared to the $y^+$ region where viscous stresses are important, which is ordinarily at the outer edge of the buffer zone, say $y^+ \sim 40$. When $Re_k$ is much less than 40 ($Re_k < 5$–10), wall roughness does not affect the viscous-stress region, the viscous sublayer is totally intact and undisturbed, and the flow is 'smooth'. In boundary layers where $Re_k$ is greater than 40 ($Re_k > 55$–90), viscous effects are negligible and the flow is 'fully rough'. When the viscous sublayer is only partially altered by the presence of roughness, the flow is 'transitionally rough'. Here, both bluff-body-form drag, and viscosity influence the near-wall flow, and log regions of mean-velocity profiles show dependence on both $\nu/U_\tau$ and $k_s$, where the former quantity is more important as 'smooth' flow is approached, and the latter, near 'fully rough' flow conditions.

Of studies of the structure of boundary layers developing over rough surfaces, Grass

(1971) employed flow visualization to elucidate features of the ejection–sweep cycle of events. He observed that ejection of low-speed fluid away from walls and the subsequent inrush of high-speed fluid toward walls are a common flow structure regardless of boundary-roughness condition. Differences in structure result as different dominant modes of instability prevail for different wall roughnesses. Liu, Kline & Johnston (1966) also used flow visualization, but studied boundary-layer flow over $d$-type roughness consisting of square bars. Perry, Schofield & Joubert (1969), Wood & Antonia (1975), and others have also studied boundary layers developing over $d$-type roughness. The differences between $d$-type and $k$-type wall roughness are most apparent in pipe flows: wall roughness is $d$-type rather than $k$-type when flow properties scale on pipe diameter instead of roughness size.

Pimenta, Moffat & Kays (1975) and Coleman, Moffat & Kays (1977) studied characteristics of boundary layers developing over the same $k$-type rough surface used in the present study: coplanar uniform spheres packed in the most dense array. Coleman focused on fully rough layers with acceleration, whereas Pimenta studied zero-pressure-gradient flows, both with and without transpiration. Pimenta showed that normalized profiles of the longitudinal component of turbulence intensity in fully rough layers had different shapes to transitionally rough profiles measured at one freestream velocity.

Antonia & Luxton (1971) present energy balances for the turbulent kinetic energy and mean flow. From the former, the authors indicate that a large-eddy diffusion process may be relevant: large energy loss by diffusion from the inner layer being consistent with high turbulence intensity observed in the outer layer. Schetz & Nerney (1977) found that profiles of longitudinal-turbulence intensity normalized with respect to the free-stream velocity increase with either surface roughness or injection rate in a study of flow near the surface of an axisymmetric body. Andreopoulos & Bradshaw (1981) present Reynolds-stress-tensor component profiles and triple-product profiles in smooth and fully rough boundary layers. According to these authors, within 3–5 roughness heights, normalized triple products are larger in fully rough flows than in flows over smooth surfaces.

Recent studies of spectra measured in flows developing over rough surfaces have been made by Perry & Abell (1977), Champagne (1978), and Sabot, Saleh & Comte-Bellot (1977). Perry & Abell (1977) studied flow in pipes with hexagonal weave roughness, and showed that, for $y^+ > 100$, rough-wall spectra can be predicted from smooth-wall results by properly scaling the measurements. Champagne (1978) made measurements in a variety of flows, including atmospheric boundary layers developing over surfaces with known roughness characteristics. He demonstrated that fine-scale structures of turbulent velocity fields are consistent with Kolmogorov's normalized spectral shapes when compared at appropriate values of the turbulence Reynolds number $Re_\lambda$. Sabot *et al.* (1977) report the results of a study of the effects of roughness on the intermittent maintenance of Reynolds shear stress in pipe flow. In their paper, the authors indicate that the mean shear stress is maintained primarily by ejection events. When compared with smooth-wall flows, ejection in rough-wall-pipe flows have larger mean periods of occurrence, larger mean time duration and lengthscale, and larger negative instantaneous shear-stress peaks.

The present paper describes measurements in transitionally rough and fully rough turbulent boundary layers over a range of roughness Reynolds numbers. In §2, details of the experimental facility and measurement techniques are given. In §3, attention is focused on the behaviour of hydrodynamic and thermal log region mean-profile

shifts. In §4, profiles of turbulence kinetic energy, turbulence kinetic-energy production, and the Reynolds-stress-tensor components are presented and discussed. Results from the present study are also related to other workers' observations of the ejection–sweep cycle of events. Section 5 contains a discussion of one-dimensional spectra, which allow conclusions to be drawn regarding spectral shapes in boundary layers developing over rough and smooth walls. Finally, concluding remarks are presented in §6.

## 2. Experimental facility and techniques

The wind tunnel used was the HMT roughness rig described by Pimenta *et al.* (1975), Ligrani, Moffat & Kays (1979), and also by Coleman *et al.* (1977), who provide a photograph of the rough surface. The test surface of the facility is 2.44 m long and consists of 24 plates, which can be electrically heated individually to maintain given temperature or transpiration boundary conditions. Each plate consists of 11 layers of 1.27 mm diameter oxygen-free, high-conductivity copper spheres packed in the most dense array and brazed together. According to Schlichting's (1968) tabulations for various sizes and shapes of roughness, the uniform spheres roughness has an equivalent sandgrain roughness size of 0.79 mm. Using fully rough velocity-profiles information, this was confirmed by Pimenta *et al.* (1975). The wind tunnel is closed-circuit, with a Plexiglas top wall which is flexible for alteration of free-stream velocity. For the present tests the top wall was adjusted to produce a zero pressure gradient along the test surface to within 0.5 mm of water for free-stream velocities from 10.1 m/s to 27.8 m/s. With devices which may be installed just upstream of the test section, the boundary layers in the wind tunnel may be artificially thickened (Ligrani & Moffat 1979; Ligrani, Moffat & Kays 1983). These devices were employed in the present study to produce layers having momentum thickness greater than 0.70 cm.

Experimental results are given for five different free-stream velocities. For the range of boundary thicknesses examined, transitionally rough behaviour exists at free-stream velocities of 10.1, 15.8 and 20.5 m/s, and fully rough behaviour exists when the free-stream velocity equals 26.8, and 39.5 m/s. Thus, in contrast to Grass' study where $Re_k$ was altered by changing roughness size, $Re_k$ is altered in the present study by changing the free-stream velocity. Experimental conditions for the presented Reynolds-stress-tensor component profiles are tabulated in table 1, where $U_\infty$ is the mean free-stream velocity, $\delta_2$ is the momentum thickness, $Re_{\delta_2}$ is the momentum-thickness Reynolds number, and $U_\tau$ is the friction velocity. Apparent downstream locations, determined from momentum-thickness measurements (Ligrani *et al.* 1979), are denoted $x_2$ and are also given in table 1.

The wall heat flux was determined by energy balances on each segment of the plate. The power input to each segment was measured and then losses were subtracted to determine magnitudes due to convection on one side of a plate. Test-surface segments in the wind tunnel are each instrumented with thermocouples for wall-temperature measurements and energy-balance calculations. For all heat-transfer measurements, the wall temperature was maintained uniform within $\pm 0.1$ °C, with free-stream to wall temperature differences of approximately 20 °C. Mean fluid temperatures were measured using a chromel–constantan thermocouple mounted on a traversing mechanism with a micrometer for adjustment of probe positions from the wall. Free-stream temperatures were measured using an iron–constantan thermo-

| Symbol | $U_\infty$ (m/s) | $\delta_2$ (cm) | $Re_k$ | $Re_{\delta_2}$ | $U_\tau$ (m/s) | $x_2$ (m) |
|---|---|---|---|---|---|---|
| ● | 26.8 | 0.56 | 63.0 | 9570 | 1.247 | 1.78 |
| ▼ | 20.4 | 0.52 | 46.7 | 6710 | 0.940 | 1.78 |
| ▲ | 15.8 | 0.53 | 36.7 | 5440 | 0.722 | 1.78 |
| ■ | 10.1 | 0.50 | 22.8 | 3310 | 0.425 | 1.78 |
| ⊙ | 26.8 | 1.08 | 61.4 | 18700 | 1.206 | 4.61 |
| ▽ | 20.4 | 1.03 | 44.4 | 13590 | 0.879 | 4.66 |
| △ | 15.8 | 1.03 | 34.6 | 10650 | 0.680 | 4.75 |
| ⊡ | 10.1 | 0.95 | 20.5 | 6310 | 0.393 | 4.64 |

TABLE 1. Summary of measurement conditions

couple probe. All temperature probes were calibrated in a Rosemount Model 910A Temperature Calibration Oil Bath, using Hewlett–Packard Model 2801A Quartz Thermometer as a standard.

Local skin-friction coefficients were determined from the Reynolds shear stresses and mean velocities, measured in the near-wall region, using

$$\tfrac{1}{2}C_f = \frac{(-\overline{u'v'})_y}{U_\infty^2} + \frac{\nu}{U_\infty^2}\frac{\partial U}{\partial y}\bigg|_y + \frac{U(y)}{U_\infty^2}\frac{\partial}{\partial x}\int_0^y U\,\mathrm{d}y - \frac{1}{U_\infty^2}\frac{\partial}{\partial x}\int_0^y U^2\,\mathrm{d}y,$$

where $-\overline{u'v'}$ is the Reynolds shear stress, and $U$ is mean velocity, where subscript $\infty$ denotes free stream. This equation was derived using the boundary-layer equation integrated from the wall to the position $y$. The distance above the crests of the roughness elements used for determination of $\frac{1}{2}C_f$ was 0.330 cm due to limitations on hot-wire probe size. For all cases investigated, $-\overline{u'v'}/U_\infty^2$ measured at $y = 0.330$ cm was 96–98 % of $\frac{1}{2}C_f$. Total wall shear stress is denoted by $\tau_w$, and local total shear stress is denoted by $\tau$. Skin-friction coefficients determined with this method were in good agreement with those determined from $\delta_2$ measurements and the two-dimensional momentum integral equation ($\frac{1}{2}C_f = \mathrm{d}\delta_2/\mathrm{d}x$), showing a maximum deviation of only a few per cent.

The $y$ origin for mean-velocity profiles was determined using the method of Monin & Yaglom (1971), which gives the same result as the method described by Perry *et al.* (1969). A corrected roughness size $z_0$ is assumed to be invariant as $y'$ is changed near the wall in a fully rough flow field. $z_0$ is defined using

$$U^+ = \frac{1}{\kappa}\ln\left[\frac{y' + \Delta y}{z_0}\right],$$

where $\kappa = 0.41$, $y'$ is measured from the roughness-element crests, and $\Delta y$ is the distance between crests and the velocity-profile origin below the crests. Perry *et al.* (1969) describe their technique for fully rough flows as one where a trial-and-error procedure is used to calculate a $\Delta y$ to give velocity-profile log-region data which is straight with the appropriate slope. In the Monin & Yaglom method, fully rough velocity-profile data follow straight lines when $z_0$ is invariant between different positions in a profile. The velocity-profile origin is then $y = 0$, and hence $y = y' + \Delta y$. In the present study, a $\Delta y$ of 0.023 cm was determined at all fully rough measuring stations and then used for profiles at all measurement conditions. These methods do not allow determination of $\Delta y$ in transitionally rough flows for $y^+ < 40$ because viscous effects cause mean profile $U^+$ data to deviate from a linear dependence on $\log y$. However, the fully rough $\Delta y$, 0.023 cm, gives transitionally rough log-region profile data which follow straight lines when $y^+$ is greater than 40.

The mean velocity $U$ and six Reynolds-stress-tensor components $\overline{u'^2}$, $\overline{v'^2}$, $\overline{w'^2}$, $-\overline{u'v'}$, $\overline{v'w'}$, and $\overline{u'w'}$, were measured using standard hot-wire anemometer techniques (Ligrani *et al.* 1979). Two types of probes were employed, a DISA 55F04 horizontal wire and a DISA 55F02 slant wire, both mounted on traversing mechanisms similar to the one used for mean-temperature profiles. The sensing length of the horizontal wire was 1.25 mm, the slant-wire probe sensing length was slightly longer. A 0.45 mm long DISA 55A53 probe was also used to measure $u$ spectra and to check spanwise uniformity with respect to individual roughness elements. The probes were used with TSI Model 1050 bridges operated in constant-temperature/constant-resistance mode with wire overheat ratios of 1.5. The bridges were connected to TSI Model 1052 linearizers, followed either by a Hewlett–Packard Model 2401 C integrating digital voltmeter for mean voltage, or a TSI model 1076 r.m.s. meter for r.m.s. values of the fluctuating voltage. The directional sensitivity of the hot-wire probes was described using Jorgensen's (1971) equations. Five different rotational positions of the slant-wire probe were used in conjunction with horizontal-wire measurements to determine the six Reynolds-stress-tensor components. The hot-wire measurements were made when the flow field was isothermal at the same temperature as was used for calibration and, thus, no temperature corrections were required.

Spectra of the longitudinal velocity fluctuations were measured using digital data-sampling techniques and fast Fourier transforms. After leaving the hot-wire anemometer bridge and linearizer, the output was filtered to remove signals above 8 kHz to prevent aliasing. A Hewlett–Packard 2440A analog–digital interface was then used to sample the signal at 20 kHz with a resolution of 12 bits. A set of 2048 samples was taken from the signal using a program on a Hewlett–Packard 2100 minicomputer, which first passes the samples through a Hamming data window and then discrete-Fourier-transforms each sample. The resulting spectra were averaged in ensembles of 64 to decrease statistical error. For each measurement, $\overline{u'^2}$ values determined from the spectra showed excellent agreement with analog values measured after the hot-wire linearizer.

Local turbulence-intensity levels, $(\overline{u'^2})^{\frac{1}{2}}/U$, never exceeded 30 % at horizontal-wire measuring stations, and 18 % at the slant-wire measuring stations. Thus, according to estimates made from results given by Tutu & Chevray (1975), and Kawall, Shokr & Keffer (1983), mean-velocity and Reynolds-stress-tensor component error estimates lie within uncertainty intervals given by Ligrani *et al.* (1983): $U$, $\pm 2$ %; $\overline{u'^2}$, $\pm 5$ %; $\overline{v'^2}$, $\overline{w'^2}$, $-\overline{u'v'}$, $\pm 10$ %. These uncertainty estimates are valid for quantities measured with 1.25 mm long sensors, which may give spatially filtered signals for small $y/\delta$. Discussion of spatial filtering is given later in this section and in the Appendix.

Within at least one roughness height of the surface, some periodicity in the flow would be expected due to the 'wavelike' character of the packed roughness elements, where the wavelength of the flow variations is on the order of the distance between the peaks of roughness elements. The 1.25 mm long horizontal wire was chosen to provide a spanwise average of these variations. Measurements on the tunnel centreline, and at 7.62 cm on either side of the centreline showed $\overline{u'^2}$ and mean velocity to be spanwise uniform for $y^+/Re_k > 0.61$. Measurements with the slant wire for $y^+/Re_k > 4.3$ provided additional evidence of a two-dimensional flow field since profiles of $\overline{w'^2}$, $-\overline{u'v'}$ and $\overline{v'^2}$ were spanwise uniform, and because $\overline{u'w'}$ and $\overline{v'w'}$ were negligible compared with $-\overline{u'v'}$. These spanwise uniformity checks were made at locations where boundary momentum thickness equalled 0.558 cm, 0.864 cm, and 1.038 cm. Measurements at three different locations with respect to one roughness element (above the crest, two different locations above troughs) were also made with the 0.45 mm long sensor; however, because of the probe configuration, it was placed

only as close to the wall as $y^+/Re_k = 4.3$, and no three-dimensional, time-averaged flow variations were observed.

Because it was desired that hot-wire sensors average any wavelike motion from roughness periodicity in the time-averaged flow near roughness elements, 1.25 mm long sensors were used for measurement of the time-averaged Reynolds-stress-tensor components. Because the 1.25 mm sensor spanwise averages, it also spatially filters. For this reason, 0.45 mm and 3.00 mm long sensors (in addition to the 1.25 mm sensor) were used to measure $u$-spectra and to check the effect of 'eddy-averaging' due to the finite spatial resolution of hot-wire sensors at $U_\infty = 26.8$ m/s and $Re_{\delta_2} = 9570$.

The Appendix shows:

(i) At $y'/\delta = 0.078$ ($y^+ = 261$), the magnitude of measured $\overline{u'^2}$ increases by 12% as $l$ changes from 3.00 mm ($l^+ = 234$) to 1.25 mm ($l^+ = 97$), and by 13% as $l$ changes from 1.25 mm to 0.45 mm ($l^+ = 35$). Here, $l^+ = lU_\tau/\nu$, where $l$ is the length of the hot-wire sensor.

(ii) In locally isotropic turbulence, normalized $u$-spectra measured with sensors having different lengths are consistent with results given by Wyngaard (1968).

(iii) According to Wyngaard (1968), at $y/\delta = 0.078$ ($y^+ = 261$), the 0.45 mm long sensor gives $\overline{u'^2}$ which are 1.1% less than if a sensor having totally adequate spatial resolution is employed.

Thus, in inner-boundary-layer regions, $\overline{u'^2}$ measured with a 1.25 mm long sensor are less than those obtained using a probe having totally adequate spatial resolution. The results given in §4 (and previously given uncertainty estimates) are presented within this context: all are consistent with each other, having the same amount of spatial filtering with respect to 1.25 mm wire length.

The fully rough $\overline{u'^2}$ variations with $l^+$ at $y^+ = 261$ are less than those observed near smooth walls by Willmarth & Sharma (1984) at $y^+ = 13.3$, and by Johansson & Alfredsson (1983) at $y^+ \sim 16$. This is because the amount of 'eddy-averaging' from hot-wire sensors having finite spatial resolution is dependent upon the spanwise extent of energy-containing eddies. Overall energy levels determined from spatially filtered, dimensional wavenumber spectra depend on the shape and magnitude of the true spectra, which may vary at different $y^+$ and with surfaces roughness, particularly very near walls.

Wyngaard (1968) shows how spatial filtering occurs from hot-wire sensors when the true spectrum follows Pao's (1965) formulation, valid for small-scale motions which are locally isotropic. When Reynolds numbers based on Taylor microscale $Re_\lambda$ are less than about 100, shapes of true longitudinal velocity spectra may be significantly different than Pao's equations. In particular, spectra may not have inertial subranges. As a result, spatial filtering from hot-wires may vary from Wyngaard's results. This is demonstrated by work by the first author at one $Re_\lambda$ less than 100, where $u$ spectra show larger variations with non-dimensional wire length than given by Wyngaard.

## 3. Scalar quantities and mean profiles

In log regions of velocity profiles over rough and smooth walls,

$$U^+ = \frac{1}{\kappa} \ln\left[\frac{y}{k_s}\right] + B, \tag{1}$$

where the value of $B$ varies with $Re_k$ and roughness-geometry characteristics. Above an upper critical value of the roughness Reynolds number, $Re_{k,\mathrm{R}}$, the value of $B$ is

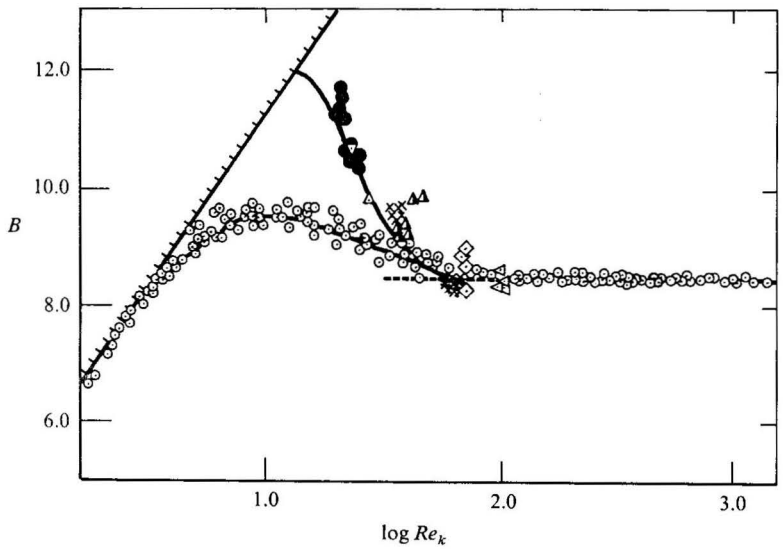


FIGURE 1. Variation of log-region velocity-profile parameter $B$ with roughness Reynolds number: ⊙, sandgrain roughness, Nikuradse (1933); ▽, ●, $U_\infty = 10.1$ m/s; △, ▲, ×, $U_\infty = 15.8$ m/s; ◇, *, $U_\infty = 26.8$ m/s; ◁, $U_\infty = 39.6$ m/s; ◁, ◁, Healzer *et al.* (1974); ▲, ◇, ◁, Pimenta *et al.* (1975); ◓, ×, *, present study. ——, $B = 1/\kappa \ln(Re_k) + 5.1$, smooth-wall flow; ---, $B = 8.5$, fully rough flow; ——. equations (6) and (7), transitionally rough flow.

constant and the flow is fully rough. According to Pimenta *et al.* (1975), for fully rough boundary layers over uniform spheres roughness, and Schlichting (1968), for fully rough flows in pipes with sandgrain roughness,

$$B = 8.5. \tag{2}$$

There is also a lower critical value, $Re_{k,\mathrm{s}}$, below which the flow obeys the smooth-wall law of the wall. If $Re_k < Re_{k,\mathrm{s}}$, $B$ has the form

$$B = \frac{1}{\kappa} \ln(Re_k) + C, \tag{3}$$

where $C$ is a constant equal to 5.10. For $Re_{k,\mathrm{s}} < Re_k < Re_{k,\mathrm{R}}$ the flow is transitionally rough and, according to Clauser (1956) and Rotta (1962), $B$ is then a function of $Re_k$ and roughness geometry.

Log regions of velocity profiles over smooth and rough walls may also be described using

$$U^+ = \frac{1}{\kappa} \ln\left[y \frac{U_\tau}{\nu}\right] + C - \frac{\Delta U}{U_\tau}, \tag{4}$$

where $C$ retains its smooth-wall value and the velocity-profile shift, $\Delta U/U_\tau$, equals zero for smooth-wall flows. From (1), for flows over rough surfaces,

$$\frac{\Delta U}{U_\tau} = C - B + \frac{1}{\kappa} \ln\left[\frac{k_\mathrm{s} U_\tau}{\nu}\right]. \tag{5}$$

Thus $\Delta U/U_\tau$ is the difference between log regions of rough-wall mean-velocity profiles and the smooth law of the wall. From (5) it is evident that the velocity-profile shift from the smooth law of the wall is dependent on $B$ and $Re_k$. This approach was first suggested by Nikuradse (1933) for flows in pipes and by Hama (1954) for boundary layers. Clauser (1956), Rotta (1962), and Schlichting (1968) also discuss the velocity profile shift.

### 3.1. *Transitionally rough hydrodynamic law of the wall*

Using (1), the values of $B$ can be determined from boundary-layer velocity profiles. Values of $B$ versus $Re_k$ for the roughness of the present boundary-layer study, from Pimenta *et al.*'s (1975) study, and from Healzer, Moffat & Kays' (1974) study (uniform spheres) are plotted in figure 1, along with $B$ versus $Re_k$ data for sandgrain roughness in pipes from Nikuradse (1933) (also see Schlichting 1968). As is evident from figure 1, data for both types of roughness can be presented by the parameter correlation

$$B = C + \frac{1}{\kappa}\ln(Re_k) + \left[8.5 - C - \frac{1}{\kappa}\ln Re_k\right]\sin(\tfrac{1}{2}\pi g), \tag{6}$$

where

$$g = \frac{\ln(Re_k/Re_{k,\mathrm{s}})}{\ln(Re_{k,\mathrm{R}}/Re_{k,\mathrm{s}})}, \quad \text{for } Re_{k,\mathrm{s}} < Re_k < Re_{k,\mathrm{R}}, \tag{7a}$$

$$g = 1, \quad \text{for } Re_k > Re_{k,\mathrm{R}}, \tag{7b}$$

and

$$g = 0, \quad \text{for } Re_k < Re_{k,\mathrm{s}}. \tag{7c}$$

In the transitionally rough regime, both the data and (6) approach fully rough behaviour as $Re_k$ increases. As $Re_k$ decreases, the value of $B$ increases for the spheres roughness, indicating an approach to smooth behaviour represented by (3). For uniform-spheres roughness, $Re_{k,\mathrm{R}} = 55.0$ and $Re_{k,\mathrm{s}} = 15.0$ were used in (6) and (7), whereas $Re_{k,\mathrm{R}} = 90.0$ and $Re_{k,\mathrm{s}} = 2.25$ are recommended for sandgrain roughness.

For the uniform-spheres roughness, figure 1 shows that transitionally rough behaviour occurs over a smaller range of $Re_k$ than for the sandgrain roughness. The quicker change from smooth to fully rough behaviour occurs as a result of the uniformity of the spheres roughness in contrast to the more gradual transition caused by sandgrains having a more irregular distribution of sizes and shapes. However, both types of behaviour are well represented by (6) and (7), where the different geometric characteristics of the two types of roughness are taken into account using appropriate values of $Re_{k,\mathrm{R}}$ and $Re_{k,\mathrm{s}}$. $Re_{k,\mathrm{R}}$ and $Re_{k,\mathrm{s}}$ are thus fixed by the roughness geometry, where the dependence of $Re_{k,\mathrm{R}}$ and $Re_{k,\mathrm{s}}$ on roughness geometry may most likely be expressed in terms of the standard deviation of the variation of size, and shape of a given roughness. The more uniform the roughness, the larger $Re_{k,\mathrm{s}}$ and the smaller the difference between $Re_{k,\mathrm{R}}$ and $Re_{k,\mathrm{s}}$.

Examples of transitionally rough ($15 < Re_k < 55$) and fully rough ($Re_k > 55$) mean-velocity profiles are shown in $U^+$ versus $y^+$ coordinates in figure 2. The smooth law of the wall and the equation $U^+ = y^+$ are also shown on the figure. The mean-profile data have distinct log regions over a range of $y^+$. For larger $y^+$, the profiles in figure 2 diverge from straight lines as wake behaviour is encountered in the outer parts of the boundary layers. $U^+$ versus $y^+$ coordinates are most appropriate for showing differences between smooth and transitionally rough mean-velocity profiles, since log regions of smooth-wall data collapse on one line and transitionally rough data shift below the law of the wall.

The transitionally rough profiles in figure 2 contain data points for $y^+ < 40$ which lie below lines which represent log regions. These data points provide evidence that viscous stresses are important compared with stresses caused by turbulent-fluid motion. If log-region lines are extrapolated to the $U^+ = y^+$ equation, the intersection point is designated as $y^+ = A^+$, the effective viscous-sublayer thickness. $A^+$ magnitudes

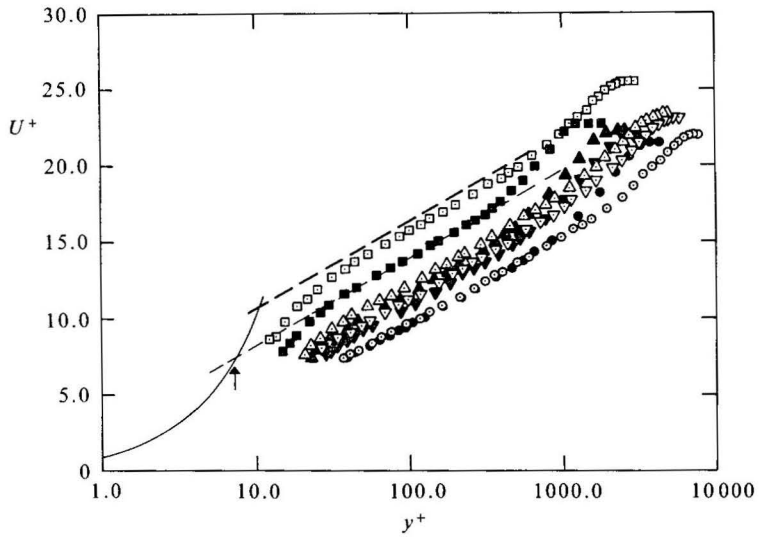


FIGURE 2. Rough-wall mean-velocity profiles, smooth-wall coordinates: data symbols given on table 1. ——, $U^+ = y^+$; — —, $U^+ = 1/\kappa \ln(y^+) + 5.1$; – –, transitionally rough log-region, $Re_k = 22.8$; ↑, $A^+$ at $Re_k = 22.8$.

are then tied to the velocity-profile shift since

$$\frac{\Delta U}{U_\tau} = C - A^+ + \frac{1}{\kappa} \ln A^+. \tag{8}$$

As the magnitude of the $\Delta U/U_\tau$ velocity-profile shift becomes less, viscous-stress regions become larger, and magnitudes of $A^+$, the effective viscous-sublayer thickness, become larger.

$A^+$ is the effective viscous-sublayer thickness which would exist if all near-wall molecular diffusion were contained in the region $y^+ < A^+$. In contrast, $\hat{A}^+$ represents the viscous-sublayer thickness if viscous stresses decrease in importance gradually with $y$, as given by the Van Driest mixing-length equation

$$l = \kappa y [1 - \exp(-y^+/\hat{A}^+)]. \tag{9}$$

Here, mixing length $l$ is defined as $(-\overline{u'v'})^{\frac{1}{2}}/|\partial U/\partial y|$. The relation between $A^+$ and $\hat{A}^+$ then follows from (8) for smooth-wall flow, which gives $A^+ = 10.8$ for $C = 5.10$. Now $\hat{A}^+$ is typically about 25 in smooth-wall boundary layers without pressure gradient, so, for that case at least,

$$\hat{A}^+ = 2.31 A^+. \tag{10}$$

$\hat{A}^+$ may then be estimated using (10), after $A^+$ is calculated from (8), where (5), (6) and (7) are used to obtain $\Delta U/U_\tau$. Near-wall mixing lengths calculated with this approach are compared with mixing lengths from mean-velocity profiles in figure 3. The equations slightly over-predict the data; however, overall trends are the same since, in both cases, $l/y$ decreases near the wall with decreasing $Re_k$. Thus the $\Delta U/U_\tau$ shift of log regions of mean-velocity profiles may be expressed in terms of changes of an empirical viscous-sublayer thickness, giving some evidence that viscous-sublayer thickness and $\Delta U/U_\tau$ velocity-profile shift are linked together.

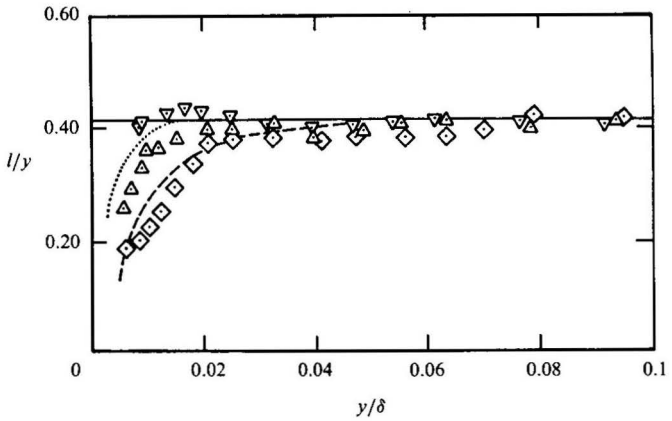


FIGURE 3. Near-wall mixing-length distributions: ▽, $Re_k = 61.4$, $U_\infty = 26.8$ m/s; △, $Re_k = 34.4$, $U_\infty = 15.9$ m/s; ◇, $Re_k = 21.0$, $U_\infty = 10.2$ m/s. Equations (9) and (10): ——, $Re_k = 61.4$; · · · ·, $Re_k = 34.0$; – – – –, $Re_k = 21.0$.

### 3.2. *Transitionally rough thermal law of the wall*

Even though turbulent diffusion is important in flow very near roughness in a fully rough flow, the only thermal-transport mechanism in the fluid immediately adjacent to rough surfaces is molecular conduction. This conducting fluid is contained in a thin film, called a conductive sublayer, which covers roughness elements and fills cracks between elements (Owen & Thomson 1963; Dipprey & Sabersky 1963). The non-dimensional temperature drop across the conductive sublayer is given by

$$(\delta t_0)^+ = \frac{(T_w - T_{cs})\,\rho c U_\tau}{q_w}, \tag{11}$$

where $T_{cs}$ is the mean temperature at the outer edge of the conductive sublayer, $T_w$ is the wall temperature, $q_w$ the wall heat flux, $\rho$ the free-stream static density, $c$ the free-stream specific heat, and $U_\tau$ the friction velocity. From experimental results, $(\delta t_0)^+$ may be estimated using

$$T^+ = (\delta t_0)^+ + Pr_t\, U^+. \tag{12}$$

With this approach for the uniform-spheres roughness of the present study,

$$(\delta t_0)^+ = k_f\, g(Re_k)^{0.20}\,(Pr)^{0.44}, \tag{13}$$

where the roughness-geometry-dependent constant $k_f$ equals 1.00. In equations (12) and (13), $T^+ = (T_w - T)/T_\tau$, where $T$ is the fluid mean temperature and $T_\tau$ is the friction temperature $q_w/\rho c U_\tau$. $Pr$ and $Pr_t$ are molecular and turbulent Prandtl numbers, respectively. Equation (13) is empirical, determined from a match to data, and based on an equation suggested by Dipprey & Sabersky (1963) for fully rough flow, where the non-dimensionalized mean-roughness height in the original equation is replaced by $Re_k$ in this study.

Mean-temperature profiles in the log regions of turbulent boundary layers may be described in terms of the conductive-sublayer temperature drop and other quantities, using

$$T^+ = (\delta t_0)^+ + Pr_t\left[\frac{1}{\kappa}\ln(y/k_s) + B_{th}\right]. \tag{14}$$

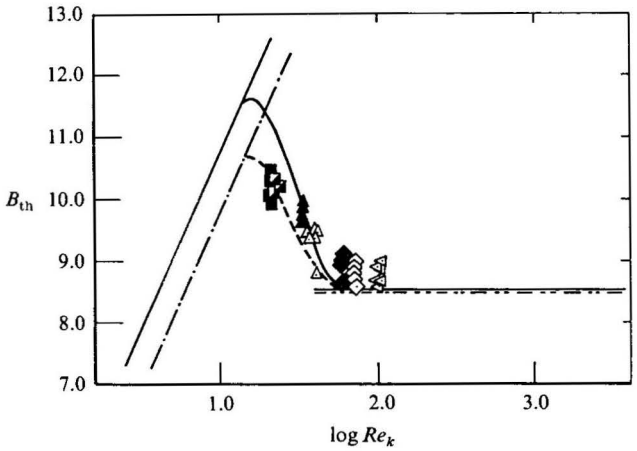


FIGURE 4. Variation of log-region temperature-profile parameter $B_{th}$ with roughness Reynolds number: ◪, ▩, $U_\infty = 10.1$ m/s; △, ▲, $U_\infty = 15.8$ m/s; ◇, ◆, $U_\infty = 26.8$ m/s; ◁, $U_\infty = 39.6$ m/s; open symbols, Pimenta *et al.* (1975); closed symbols, thermal boundary layers with unheated starting lengths. ——, $B$ versus $Re_k$ from velocity profiles; –·–·–, $B_{th} = 1/\kappa \ln(Re_k) + 4.15$, smooth-wall flow; –··–··–, $B_{th} = 8.5$, fully rough flow; – – – –, equation (16), transitionally rough flow.

For given values of $Pr$ and $Pr_t$, the temperature-profile parameter $B_{th}$ is dependent upon roughness geometry and $Re_k$. For smooth-wall flows, $(\delta t_0)^+ = 0$ and

$$T^+ = Pr_t\left[\frac{1}{\kappa}\ln(y^+) + C_{th}\right]. \tag{15}$$

According to Kays & Crawford (1980), $C_{th} = 4.15$ when $Pr_t = 0.90$ and $Pr = 0.710$.

Magnitudes of $B_{th}$ may be determined from experimental results using (13) and (14). The results of such calculations are given in figure 4. Because the temperature-profile shift is independent of unheated starting-length magnitude for thermal-boundary-layer development (Ligrani & Moffat 1985), $B_{th}$ results were obtained for thermal boundary layers both with and without unheated starting lengths. As for the hydrodynamic results in figure 1, the $B_{th}$ versus $Re_k$ distribution may be represented by a parameter correlation which asymptotically approaches smooth and fully rough behaviour at the bounds of the transitionally rough regime. This correlation, given by

$$B_{th} = C_{th} + \frac{1}{\kappa}\ln(Re_k) + \left[8.5 - C_{th} - \frac{1}{\kappa}\ln Re_k\right]\sin[\tfrac{1}{2}\pi g], \tag{16}$$

is represented in figure 4 and matches experimental data within $\pm 0.5$ non-dimensional temperature units. When the flow is fully rough and $Re_k > 55$, $B_{th}$ is approximately 8.5, as would be expected from hydrodynamic data. The hydrodynamic profile parameter $B$ is also included on figure 4, and shows a larger variation than $B_{th}$ for the range of roughness Reynolds numbers considered. However, equations for transitionally rough $B$ and $B_{th}$ are similar in form, and the measured variation of $B_{th}$ with $Re_k$ is consistent with and complementary to the variation of hydrodynamic parameter $B$ with roughness Reynolds number.

Transitionally rough and fully rough mean-temperature profiles are presented in figure 5, along with (14) for $(\delta t_0)^+ = 2.0$, $B_{th} = 8.5$ and $Pr_t = 0.90$. Even though magnitudes of $(\delta t_0)^+$ and $B_{th}$ vary between profiles, all log-region data fall on the fully

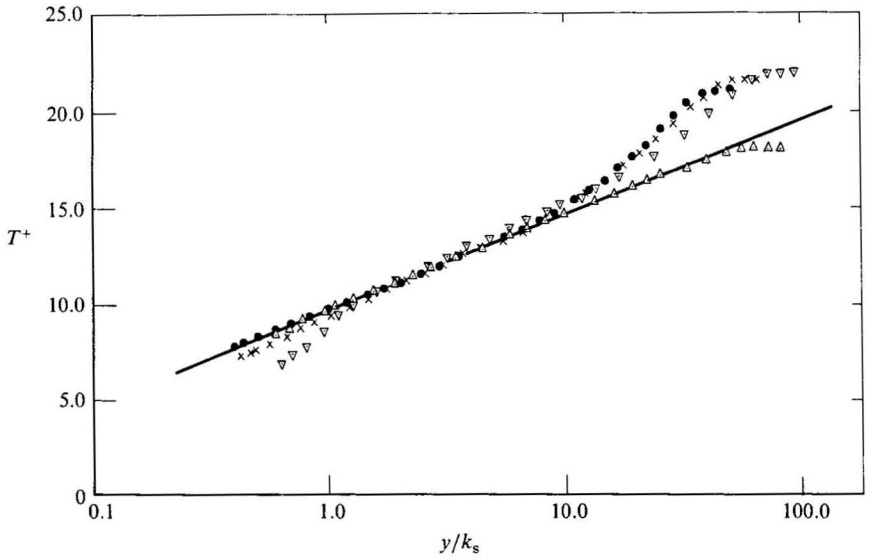


FIGURE 5. Rough-wall mean-temperature profiles, rough-wall coordinates: ●, $U_\infty = 26.8$ m/s, $Re_k = 68.4$, $\delta_2 = 0.356$ cm, $\Delta_2 = 0.353$ cm; ×, $U_\infty = 15.8$ m/s, $Re_k = 38.2$, $\delta_2 = 0.437$ cm, $\Delta_2 = 0.465$ cm; ▽, $U_\infty = 10.1$ m/s, $Re_k = 22.4$, $\delta_2 = 0.569$ cm, $\Delta_2 = 0.587$ cm; △, thermal boundary layer with 2.93 m unheated starting length, $U_\infty = 26.8$ m/s, $Re_k = 61.9$, $\delta_2 = 0.978$ cm, $\Delta_2 = 0.329$ cm. ——, equation (14) with $(\delta t_0)^+ = 2.0$, $B_{th} = 8.5$, and $Pr_t = 0.90$.

rough mean-temperature line. Such behaviour results because decreases in $(\delta t_0)^+$ are nearly cancelled by increases in the quantity $Pr_t B_{th}$ in the transitionally rough regime. Here, $\Delta_2$ represents enthalpy thickness.

For $y/k_s < 1.5$, transitionally rough data in figure 5 fall below the fully rough line by increasing amounts as $Re_k$ decreases.

## 4. Turbulence structure

Figure 6 shows profiles of $\overline{u'^2}/U_\tau^2$ versus $y'/\delta$ at different free-stream velocities and different roughness Reynolds numbers. As expected, the outer 80 % of the profiles are invariant for the range of $Re_k$ shown. If $U_\infty$ were used as a normalization parameter, the shape of the $\overline{u'^2}/U_\infty^2$ surface would be more complicated since it would vary for the range of roughness Reynolds numbers considered. For $Re_k$ greater than about 55, the $\overline{u'^2}/U_\tau^2$ profiles in figure 6 are fully rough and invariant over the outer 97–98 %. At $Re_k = 21.9$, the $\overline{u'^2}/U_\tau^2$ approaches smooth behaviour. In between the smooth and fully rough regions, the $\overline{u'^2}$ profiles are transitionally rough, and inner-region distributions of $\overline{u'^2}/U_\tau^2$ change continuously from fully rough behaviour to smooth behaviour as the free-stream velocity of the flow changes. Fully rough $\overline{u'^2}/U_\tau^2$ profiles can then be distinguished from transitionally rough profiles, since inner parts of transitionally rough profiles vary significantly as $Re_k$ changes, whereas fully rough profiles do not.

The most salient feature of fully rough $\overline{u'^2}/U_\tau^2$ profiles is a broad, flat 'hump' with a maximum value at $y^+ = 250$–$400$ or $y'/\delta \sim 0.10$. Such 'humps' are clearly evident in figure 7, where $\overline{u'^2}/U_\tau^2$ data for different $Re_k$ and different boundary-layer thicknesses are plotted versus $y^+$. The 'humps' are regions where production of longitudinal-turbulence energy is important. On the near-wall side of these regions,

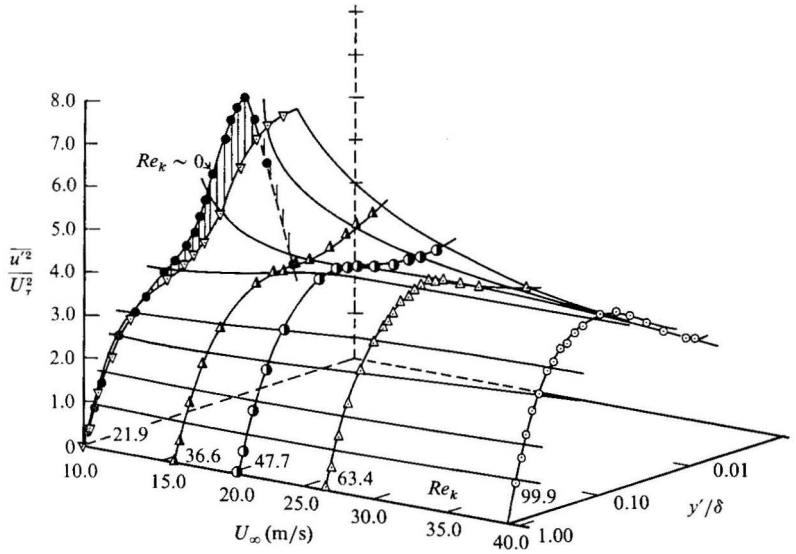


FIGURE 6. Summary of profiles of longitudinal component of turbulence intensity, normalized using the friction velocity, for smooth, transitionally rough and fully rough turbulent boundary layers: ●, Orlando *et al.* (1974), $U_\infty = 9.6$ m/s, smooth-wall flow; ⊙, Pimenta *et al.* (1975).

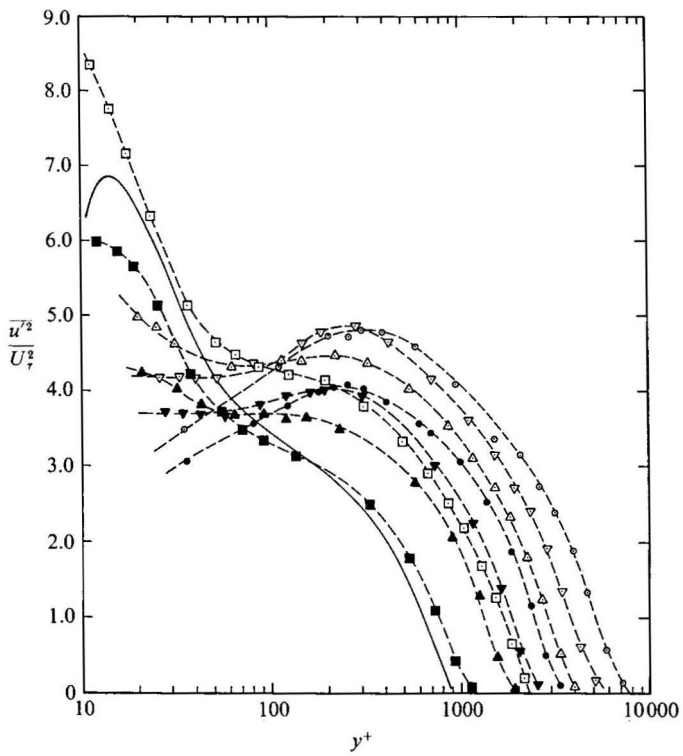


FIGURE 7. Normalized longitudinal component of turbulence intensity versus $y^+$, compared at different downstream locations and at different roughness Reynolds numbers. ——, Orlando *et al.* (1974) smooth-wall flow; other symbols shown on table 1.

$\overline{u'^2}$ increases with $y^+$. With regard to turbulent energy diffusion in a fully rough flow developing over sandpaper roughness, Andreopoulos & Bradshaw (1981) concluded that turbulent-energy sinks may exist near roughness elements so that turbulent energy is transported from inner layers toward the immediate vicinity of roughness elements. The energy balance of Antonia & Luxton (1971) near a rough surface shows that turbulent energy does not flow down gradients of turbulence kinetic energy $\overline{q^2}$ into near-wall regions, which, in the inner regions of their flow field, also indicates that transfer of energy by diffusion is not a gradient diffusion process (i.e. $\partial\overline{q^2v}/\partial y \neq V\partial\overline{q^2}/\partial y$, where $V$ is the mean velocity in the $y$-direction).

The large 'hump' in $\overline{u'^2}/U_\tau^2$ versus $y'/\delta$ profiles which characterize fully rough flow may be a result of the most important ejection–sweep cycle differences due to roughness, which, according to Grass (1971), are 'associated with the detailed mechanics of low momentum fluid entrainment at the bed surface, following inrush phases'. Entrainment near rough surfaces is much more violent than near smooth surfaces, and ejected fluid rises almost vertically from between the cavities between roughness elements. Larger amounts of low-speed fluid ($u' < 0$, $v' > 0$) may then be pushed farther from the wall to collide with inrushing high-speed flow ($u' > 0$, $v' < 0$) in larger quantities than is the case for smooth-wall flows. As a result, the region of greatest mixing is moved farther from the wall and spread over a greater portion of the layer.

In figure 7, the smooth-wall $\overline{u'^2}/U_\tau^2$ profile of Orlando, Moffat & Kays (1974) has a peak at $y^+$ about equal to 15. The transitionally rough profiles at $Re_k = 20.5$ and $Re_k = 22.8$ are similar since they also have their highest measured magnitudes near the same location. It will be shown that normalized $\overline{u'^2}$ production is maximum near $y^+ = 15$ in these transitionally rough flows, which would also be expected in boundary layers developing over a smooth surface. The two rough-wall profiles are different from Orlando's smooth-wall profile since their maxima have different values and because they do not appear to decrease with decreasing $y^+$ very near the wall.

At a given boundary-layer thickness, profiles in figure 7 intersect at one point. For $\delta_2 \sim 1.00$ cm, this intersection point lies near $y^+ = 100$, and, for $\delta_2 \sim 0.50$ cm, the point seems to be near $y^+ = 60$–$70$. For $y^+$ smaller than the intersection point, $\overline{u'^2}/U_\tau^2$ decreases with $Re_k$. The $\overline{u'^2}$ variations at these locations do not appear to approach zero as $y^+$ decreases, most likely as a consequence of finite fluid velocities at $y^+ = 0$, located between the crests and troughs of roughness elements. The $\overline{u'^2}/U_\tau^2$ profiles at $Re_k = 44.4$ and $Re_k = 46.7$ also have almost no variation with $y^+$ very near the wall. For $y^+$ larger than the intersection point, $\overline{u'^2}/U_\tau^2$ increases with $Re_k$, resulting in the fully rough 'hump' and flattened inner region transitionally rough profiles described earlier.

Variations of $\overline{u'^2}/U_\tau^2$ with $Re_k$ at $y^+$ less than the intersection point are consistent with expected changes in the viscous-sublayer thickness. If roughness size is constant, a larger percentage of roughness elements will be exposed to interact with inrushing fluid as the viscous-sublayer thickness decreases. The form drag from roughness then acts as a much more effective arrest mechanism than when fast-moving fluid near the wall is slowed only by viscous forces, as near smooth walls. When $Re_k$ is large, inrushing fluid during the ejection-sweep cycle of events is thus more greatly impeded in its longitudinal motion (Grass 1971). Such resistance to longitudinal fluid motion very near the wall increases with increasing $Re_k$ and decreasing $A^+$.

The profiles in figure 7 are again presented in $\overline{u'^2}/U_\tau^2$ versus $y'/\delta$ coordinates in figure 8. Here, the collapse of the outer parts of the profiles, regardless of $Re_k$ and boundary-layer thickness, is evident, provided $Re_{\delta_2} > 5000$. In the inner parts of the

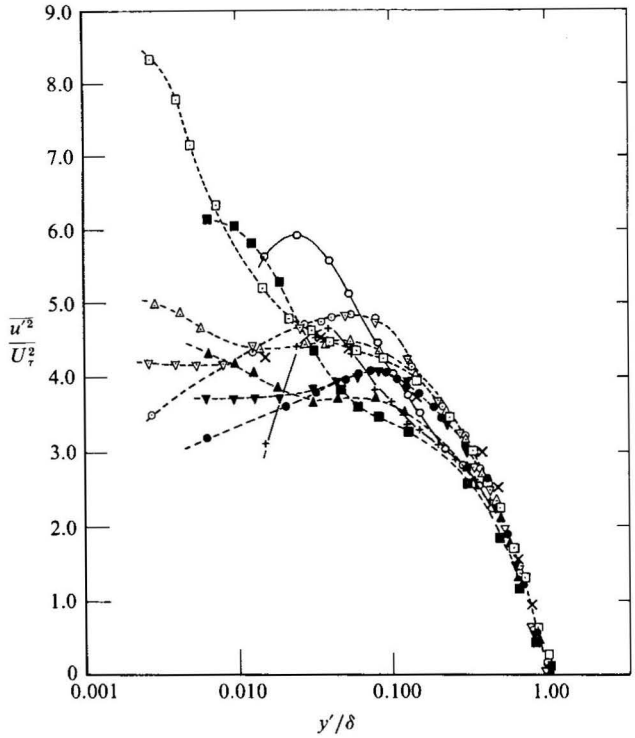


FIGURE 8. Normalized longitudinal component of turbulence intensity versus $y'/\delta$ compared at different downstream locations and at different roughness Reynolds numbers: ×, $Re_k = 310$, Andreopoulos & Bradshaw (1981); —+—, $Re_k = 84.7$, Grass (1971); —○—, $Re_k = 20.7$, Grass (1971); other symbols shown on table 1.

profiles, where normalized data points differ with $Re_{\delta_2}$ and $Re_k$, magnitudes of $\overline{u'^2}/U_\tau^2$ at a given free-stream velocity increase with $Re_{\delta_2}$. Such a trend was also observed by Pimenta *et al.* (1975) for $Re_{\delta_2} < 10^4$. Results from Grass (1971) and Andreopoulos & Bradshaw (1981) are included on figure 8. The former have different shapes and maxima at different $y'/\delta$ compared to results from the present study, whereas the latter show general qualitative agreement in terms of shape, lying between the two profiles at $Re_k = 61.4$ and $Re_k = 63.0$.

Profiles of the normal and transverse components of the Reynolds-stress tensor $\overline{v'^2}$ and $\overline{w'^2}$ are given in figure 9. These quantities are normalized using the free-stream velocity and plotted versus $y/\delta$. For $Re_k > 34$, the profiles are the same regardless of boundary-layer thickness or magnitude of $Re_k$. However, at $Re_k = 20.5$ and $Re_k = 22.8$, the profiles lie below the curve formed by data measured at higher roughness Reynolds numbers. This is partially due to low-momentum-thickness Reynolds-number behaviour at $Re_k = 22.8$ since this profile was measured at a location where $Re_{\delta_2}$ was equal to 3310. However, at $Re_k = 20.5$, the differences in the $\overline{w'^2}/U_\infty^2$ and $\overline{v'^2}/U_\infty^2$ profiles are believed to be entirely a consequence of a roughness flow regime which is closer to smooth behaviour than when $Re_k > 34$. Thus, the transitionally rough regime may be divided into two parts: one for $Re_k > 34$ where $\overline{w'^2}/U_\infty^2$ and $\overline{v'^2}/U_\infty^2$ profiles are the same as in fully rough flow, and one for $Re_k < 34$ where $\overline{w'^2}/U_\infty^2$ and $\overline{v'^2}/U_\infty^2$ profiles begin to diverge from the fully rough curve to approach smooth behaviour.

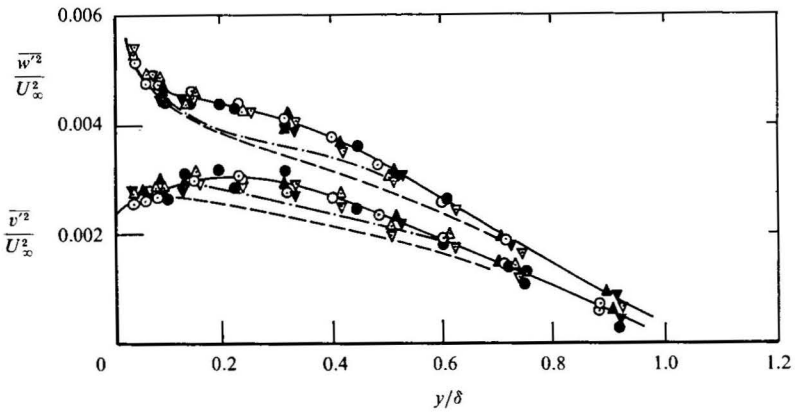


FIGURE 9. Normalized normal and transverse components of turbulence intensity versus $y/\delta$, compared at different downstream locations and at different roughness Reynolds numbers: ---, $U_\infty = 10.1$ m/s, $\delta_2 = 0.50$ cm, $Re_k = 22.8$; -·-·-, $U_\infty = 10.1$ m/s, $\delta_2 = 0.95$ cm, $Re_k = 20.5$; other symbols shown on table 1.

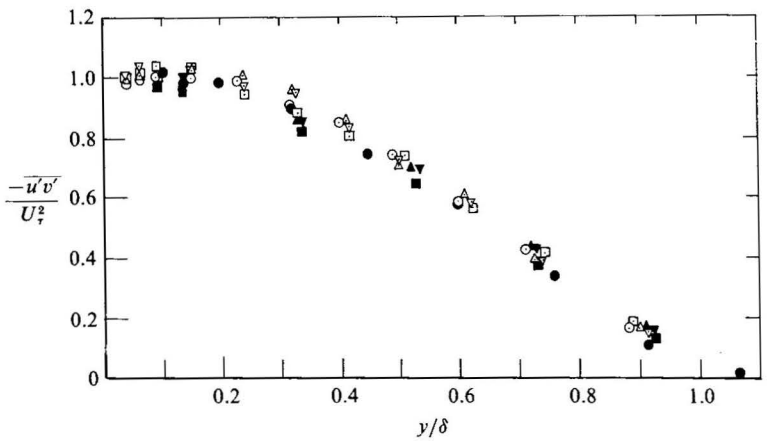


FIGURE 10. Normalized rough-wall boundary-layer Reynolds shear-stress profiles versus $y/\delta$, compared at different downstream locations and at different roughness Reynolds numbers: symbols shown on table 1.

The dependence of $\overline{w'^2}$ and $\overline{v'^2}$ on $U_\infty$ in the present study is consistent with work of Pimenta *et al.* (1975), who studied flow over the same type of roughness, but different from results from other studies. For example, in Grass' (1971) study, $\overline{v'^2}$ profiles for different $Re_k$ are invariant when scaled on $U_\tau$. In addition, magnitudes of $\overline{v'^2}$ and $\overline{w'^2}$ are, in part, a result of pressure transfer from longitudinal fluctuations and, thus, all three quantities would be expected to have some dependence on the same scaling variables. However, neither the friction velocity $U_\tau$ nor the velocity scale $(\tau/\rho)^{\frac{1}{2}}$ for the 'active', shear-stress-producing component of the turbulent motion (Bradshaw 1967*a*, *b*) collapse $\overline{w'^2}$ and $\overline{v'^2}$ profiles together.†

Profiles of the normalized Reynolds shear stress, the correlation coefficient for the Reynolds shear stress, and the ratio of the Reynolds shear stress to the turbulence kinetic energy are presented in figures 10 and 11. As expected, profiles of all three

† Some authors refer to 'active' and 'inactive' motions, as 'universal' and 'non-universal' motions, respectively.

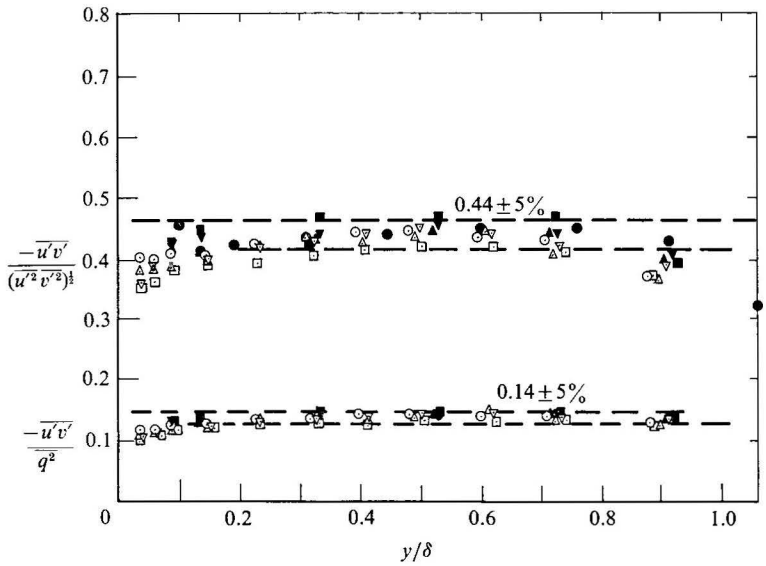


FIGURE 11. Cross-correlation coefficient for the Reynolds shear stress, and the ratio of the Reynolds shear stress to the turbulence kinetic energy, compared at different roughness Reynolds numbers and at different downstream locations: symbols shown on table 1.

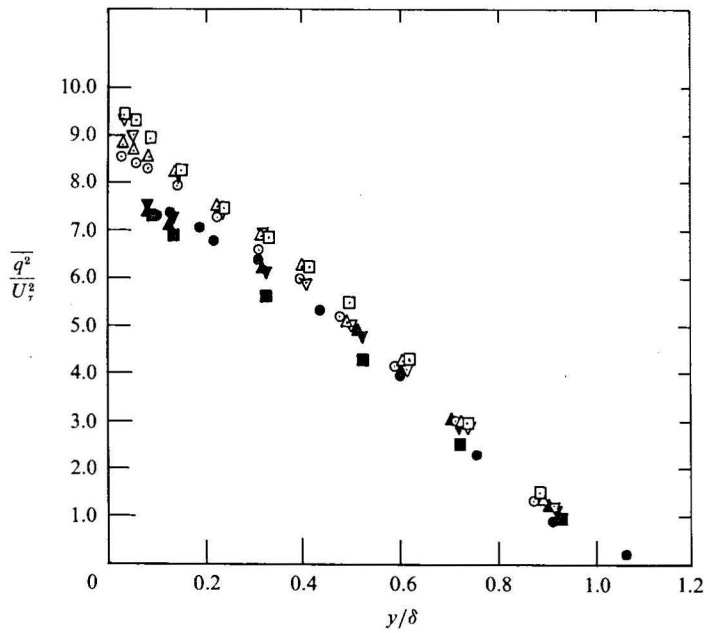


FIGURE 12. Profiles of turbulence kinetic energy, normalized using the friction velocity, versus $y/\delta$, compared at different downstream locations and at different roughness Reynolds numbers: symbols shown on table 1.

of these quantities are invariant regardless of the free-stream velocity or magnitude of roughness Reynolds number. In view of Grass' (1971) results, this suggests that the type of mechanism resulting in the production of turbulence does not change with surface roughness, even though changes in the intensity and distribution of this mechanism may occur.

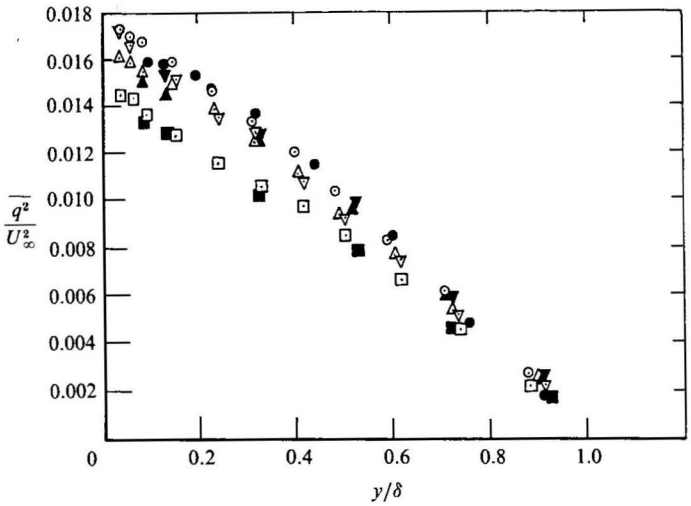


FIGURE 13. Profiles of turbulence kinetic energy, normalized using the free-stream velocity, versus $y/\delta$, compared at different downstream locations and at different roughness Reynolds numbers: symbols shown on table 1.

The turbulence kinetic energy $\overline{q^2} = \overline{u'^2} + \overline{v'^2} + \overline{w'^2}$ is now discussed referring to figures 12 and 13. Many of the qualitative trends indicated by $\overline{u'^2}$ data are also shown by the turbulence-kinetic-energy profiles. First, as for $\overline{u'^2}$ profiles, the most appropriate similarity variable for $\overline{q^2}$ profiles is the friction velocity, $U_\tau$. This is evident in figure 12, where the outer 60–70 % of $\overline{q^2}/U_\tau^2$ versus $y/\delta$ profiles show some similarity when compared at different $Re_k$ and different boundary-layer thicknesses. Such behaviour is consistent with $-\overline{u'v'}/\overline{q^2}$ data in figure 11, and the near-universal behaviour of $-\overline{u'v'}/U_\tau^2$ versus $y/\delta$. Differences in the profiles in figure 12 may be due, in part, to the dependence of $\overline{w'^2}$ and $\overline{v'^2}$ profiles on $U_\infty$.

Figure 13 shows profiles of $\overline{q^2}$ non-dimensionalized using the free-stream velocity, $U_\infty$, and plotted versus $y/\delta$. When normalized in this way, the $\overline{q^2}$ profiles show significant differences throughout the boundary layers when compared at different values of $Re_k$ and approximately the same thickness. However, the $\overline{q^2}/U_\infty^2$ versus $y/\delta$ profiles show similarity when compared at different thicknesses for a given free-stream velocity. This behaviour is dependent on the universality of $U_\tau$ normalization *and* $\frac{1}{2}C_f$ variation between compared profiles and, thus, outer regions of $\overline{q^2}/U_\infty^2$ versus $y/\delta$ profiles are not the same when compared at widely different $Re_k$.

Some understanding of the turbulence structure may be obtained by examination of equations for turbulence kinetic energy and longitudinal velocity fluctuations $\overline{u'^2}$. The equation for the balance of different quantities contributing to the magnitude of the turbulence kinetic energy is:

$$U\frac{\partial(\frac{1}{2}\overline{q^2})}{\partial x} + V\frac{\partial(\frac{1}{2}\overline{q^2})}{\partial y} + \left[\overline{u'v'}\frac{\partial U}{\partial y}\right] + \frac{\partial}{\partial y}[\tfrac{1}{2}(\overline{q^2v'}) + \overline{p'v'}] - \nu\left[\frac{\partial^2(\overline{q^2})}{\partial y^2}\right] + \epsilon = 0. \qquad (17)$$

I II III IV V VII

The equation for $\overline{u'^2}$ is:

$$U\frac{\partial\overline{u'^2}}{\partial x} + V\frac{\partial\overline{u'^2}}{\partial y} + 2\left[\overline{u'v'}\frac{\partial U}{\partial y}\right] + \frac{\partial}{\partial y}[\overline{u'^2v'}] - 2\nu\left[\frac{\partial^2\overline{u'^2}}{\partial y^2}\right] - \frac{2}{\rho}\overline{p'\frac{\partial u'}{\partial x}} + 2\epsilon_u = 0. \qquad (18)$$

I II III V VI VII

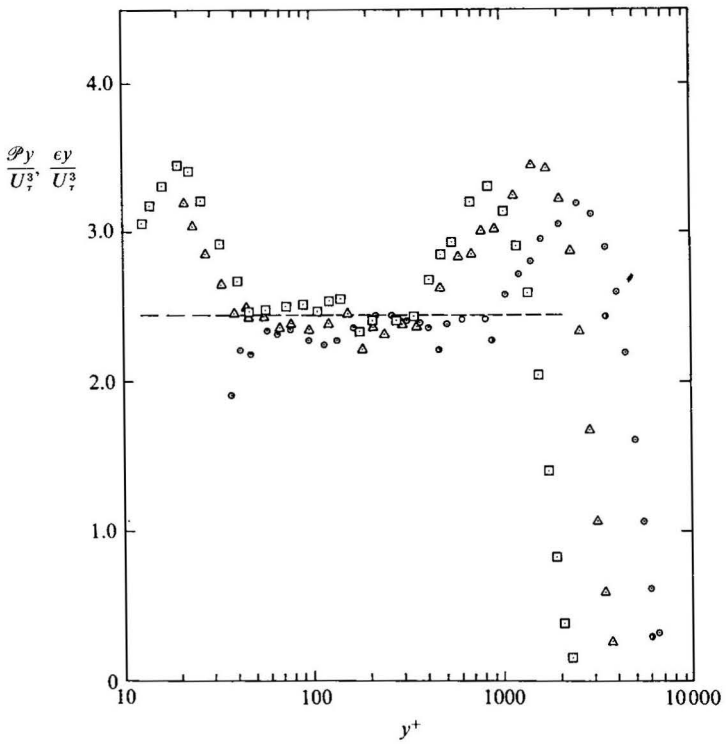


FIGURE 14. Normalized turbulence-kinetic-energy production versus $y^+$: ⊙, $U_\infty = 26.8$ m/s, $\delta_2 = 1.04$ cm, $Re_k = 61.4$; △, $U_\infty = 15.8$ m/s, $\delta_2 = 1.00$ cm, $Re_k = 34.4$; ⊡, $U_\infty = 10.1$ m/s, $\delta_2 = 0.92$ cm, $Re_k = 21.0$; ◑, dissipation from spectra inertial subrange, $U_\infty = 26.8$ m/s, $\delta_2 = 1.04$ cm, $Re_k = 61.4$; ----, equation (19).

Roman numerals refer to: I, convection by mean flow; II, production; III, turbulence diffusion; IV, pressure diffusion; V, viscous diffusion; VI, pressure–strain correlation terms; and, VII, dissipation. Even though viscous diffusion is negligible over most of the boundary-layer thickness, terms containing this quantity are included in (17) and (18) owing to its importance in the viscous sublayer for smaller $Re_k$.

The production term is $-\overline{u'v'}\,\partial U/\partial y$. In the determination of this quantity, both $-\overline{u'v'}$ and $\partial U/\partial y$ were determined from mean-velocity profiles. For the former, the total shear stress throughout the layers was calculated using integrated forms of the two-dimensional boundary-layer equations (Ligrani & Moffat 1985). The laminar component was then subtracted off in order to obtain $-\overline{u'v'}$. The resulting $-\overline{u'v'}$ calculated profiles then showed excellent agreement with turbulent shear-stress measurements such as the ones given in figure 10. Thus the present production distributions are the same as obtained from direct measurement, except that they are presented for smaller distances from the surface.

The $\mathscr{P} = -\overline{u'v'}(\partial U/\partial y)$ production term appears in equations for $\overline{q^2}$ and $\overline{u'^2}$, but not in equations for $\overline{v'^2}$ and $\overline{w'^2}$. This term is shown in figure 14, normalized using $y/U_\tau^3$ and plotted as a function of $y^+$. $\mathscr{P}$ follows the result

$$\mathscr{P} = U_\tau^3/\kappa y, \tag{19}$$

for $40 < y^+ < 400$–$1000$, as do the smooth-wall results of Bradshaw (1967*a*). Thus, with the normalization used in figure 14, non-dimensional production curves for the

inner regions of the turbulent boundary layers show some similarity. When plotted versus $y/\delta$, the normalized production curves in the outer parts of the boundary layers collapse together. The largest magnitude of inner-region normalized production in figure 14 is present at $Re_k = 21.0$ since a peak occurs near $y^+ = 20$. This is consistent with results in figure 7 where large increases in $\overline{u'^2}$ for $y^+ < 40$–$50$ indicate a source of longitudinal turbulent energy. The peak decreases in magnitude with $Re_k$, and eventually disappears when $Re_k$ is greater than 55 and the flow becomes fully rough. In fully rough flow at $Re_k = 61.4$, the magnitudes of *dimensional* production are more than one order of magnitude greater than those at $Re_k = 21.0$, with maximum magnitudes at the minimum $y^+$ where measurements were made, near roughness-element crests. Antonia & Luxton (1971) observed production in a rough-wall boundary layer is maximum very close to roughness crests; however, they also found a broad local peak at $y/\delta \sim 0.15$.

As the roughness Reynolds number increases and a flow changes from smooth to transitionally rough to fully rough behaviour, changes in the viscous-sublayer thickness will be accompanied by changes in the relative importance of terms contained in (17) and (18). Townsend (1956) discusses turbulent kinetic-energy balance near the smooth wall of a pipe flow, indicating that turbulent diffusion and pressure diffusion may be larger than production at the outer edge of the viscous sublayer, and that energy will be transferred by direct action of viscous stresses. In transitionally rough and fully rough layers, all types of diffusion are altered by roughness. The production term, $-\overline{u'v'}\,\partial U/\partial y$, increases by large amounts as $Re_k$ increases. The large amount of dissipation in the viscous sublayer diminishes as $Re_k$ increases. Changes of these terms are tied to important structural variations, such as the complicated $\overline{u'^2}$ profile alterations with $Re_k$ observed over as many as 23 sandgrain roughness heights or 14 roughness sphere diameters from the surface (figures 6–8).

## 5. Spectra and dissipation of turbulent kinetic energy

The first Kolmogorov hypothesis states that the motion of small-scale turbulent structures is determined by $\epsilon$, the viscous dissipation of turbulent energy, and by $\nu$, the kinematic viscosity. One-dimensional spectra at large values of $k_1$, the one-dimensional wavenumber, should then be similar when normalized such that

$$\frac{f_u(k_1)}{v^2\eta} = \frac{f_u(k_1)}{(\epsilon\nu^5)^{\frac{1}{4}}} = f(k_1\eta), \tag{20}$$

where $\eta = (\nu^3/\epsilon)^{\frac{1}{4}}$ is the Kolmogorov lengthscale and $v = (\nu\epsilon)^{\frac{1}{4}}$ is the Kolmogorov velocity scale. $k_1$ is the component of the wavenumber vector $\boldsymbol{k}$ in the flow direction. It is determined from local mean velocity and frequency $n$, using $k_1 = 2\pi n/U$. The first Kolmogorov hypothesis is valid for locally isotropic flow over an equilibrium range of wavenumbers when the turbulent Reynolds number $Re_\lambda$ is greater than 40–100, where

$$Re_\lambda = \frac{(\overline{u'^2})^{\frac{1}{2}}\lambda}{\nu},$$

and $\lambda$ is the Taylor microscale.

The second Kolmogorov hypothesis concerns the behaviour of a range of wavenumbers (within the equilibrium range) called the inertial subrange. In the inertial

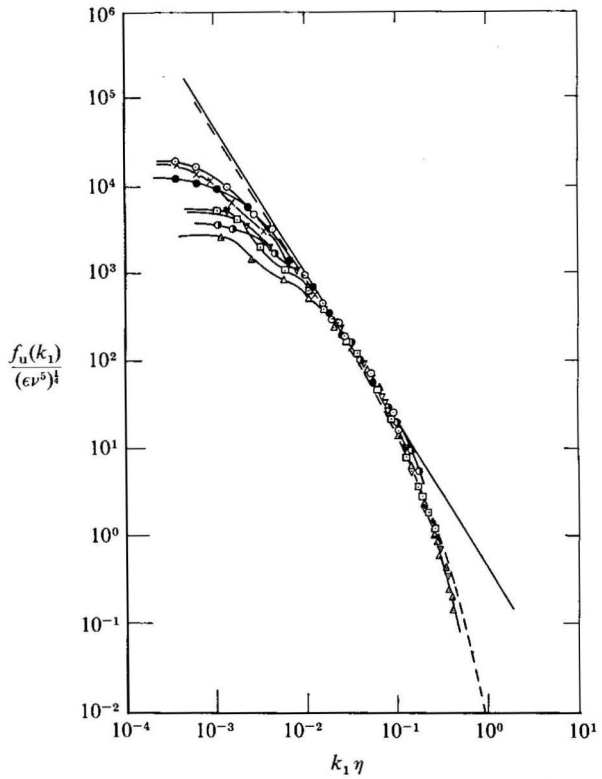


FIGURE 15. Spectra of longitudinal turbulence intensity normalized using Kolmogorov length and velocity scales in a fully rough turbulent boundary layer, $U_\infty = 26.7$ m/s, $\delta_2 = 0.558$ cm, $Re_k = 63.0$; ×, $y'/\delta = 0.078$; ⊙, $y'/\delta = 0.150$; ●, $y'/\delta = 0.60$; ◑, $y'/\delta = 1.00$. Smooth-wall channel flow: ⊡, $y/\delta = 0.086$; ▽, $y/\delta = 0.625$; △, $y/\delta = 1.00$. ---, Pao (1965); ——, equation (22) with $\alpha_1 = 0.47$.

subrange, negligible dissipation occurs, and the total energy flux across each wavenumber is constant and equal to the dissipation rate $\epsilon$. The spectra are given by

$$f_u(k_1) = \alpha_1 \epsilon^{\frac{2}{3}} k_1^{-\frac{5}{3}}, \tag{21}$$

or, alternatively,

$$\frac{f_u(k_1)}{(\epsilon\nu^5)^{\frac{1}{4}}} = \alpha_1 (k_1\eta)^{-\frac{5}{3}}, \tag{22}$$

where $\alpha_1$ is a universal constant. From Pao's (1965) results, $\alpha_1$ was estimated to be equal to 0.47. Townsend (1976) suggests $0.50 \pm 0.05$.

Spectra of the longitudinal velocity fluctuations, measured in a fully rough turbulent boundary layer at $Re_k = 63.0$ and $\delta_2 = 0.558$ cm, are presented in figure 15. Examples from a smooth-wall channel flow (centreline velocity = 14.2 m/s) are also included. On this graph, $f_u(k_1)$ represents the $\overline{u'^2}$ energy per unit $k_1$ and, thus,

$$\int_0^\infty f_u(k_1)\,\mathrm{d}k_1 = \overline{u'^2}. \tag{23}$$

In figure 15, $f_u(k_1)$ is non-dimensionalized using Kolmogorov scales, where the magnitudes of the Kolmogorov scale, as well as $\epsilon$, the dissipation of turbulent kinetic energy, were estimated using (21) with $\alpha_1 = 0.47$. Consequently, the spectra in

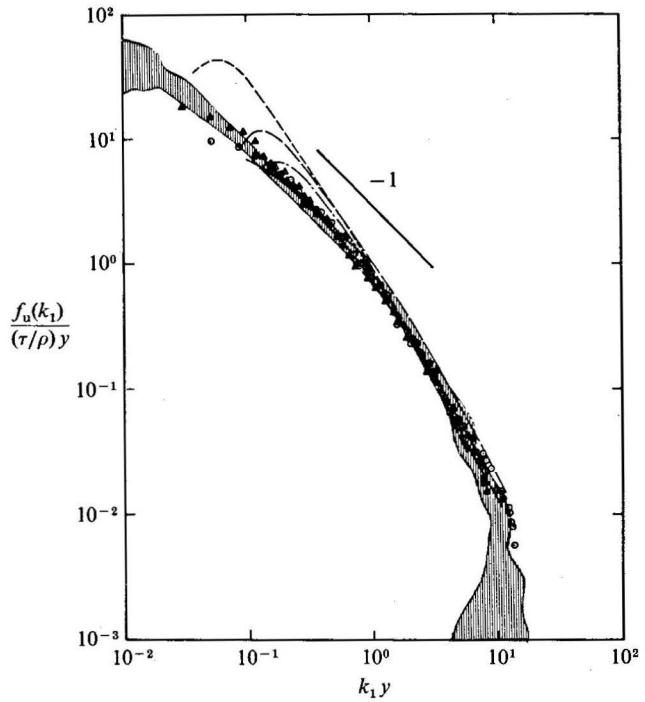


FIGURE 16. Normalized inner-layer frequency spectra, same measurement conditions as figure 15: △, $y'/\delta = 0.078$, $y^+ = 261$; ⊙, $y'/\delta = 0.150$, $y^+ = 485$. Smooth-wall boundary layer, Bradshaw (1967*b*): ——, $a = 0$, $y/\delta = 0.20$; – – – –, $a = -0.255$, $y/\delta = 0.18$; – – –, $a = -0.255$, $y/\delta = 0.11$; – – –, $a = -0.255$, $y/\delta = 0.044$. ▥, Perry & Abell (1977): smooth-wall pipe flow, $f_u(k_1)/U_\tau^2 y$ versus $k_1 y$-coordinates.

figure 15 are forced to agree with (21) and (22) in the inertial subrange. Agreement with Pao's (1965) equation for isotropic turbulence is good at higher wavenumbers, and has not been forced except by relying on (21). At wavenumbers below the inertial subrange, spectra vary because of differences in the energy contained in the large-scale structures. Because magnitudes of the Kolmogorov lengthscale in the fully rough flow are about half those in the smooth channel flow (when compared at the same $y/\delta$), fully rough spectra in $\{f_u(k_1)\}/(\overline{u'^2})$ versus $k_1$-coordinates reveal a larger percentage of energy at higher wavenumbers. If $\mathscr{P} \sim \epsilon$ in inner regions, this is consistent with (19) since the fully rough flow has larger $U_\tau$.

Magnitudes of the dissipation of turbulent kinetic energy, determined from spectra inertial subranges, are given in figure 14 for a fully rough turbulent boundary layer at $Re_k = 61.4$ and $\delta_2 = 1.04$ cm. At $y^+ = 472$ and 891, the estimated dissipation is 7–10 % lower than production. At $y^+ = 3500$ and 5850, dissipation values are again slightly lower than production; however, considering the uncertainty of the dissipation calculations, $\mathscr{P} \sim \epsilon$ at all four locations where spectra were measured in this flow.

Appropriate velocity and lengthscales for the 'active' motion portions of inner regions of turbulent boundary layers are $(\tau/\rho)^{\frac{1}{2}}$ and $y$, respectively. Fully rough spectra measured at $y^+ = 261$ and $y^+ = 485$ are presented in figure 16 non-dimensionalized using these scales. Because $\tau$ is constant and equal to $\tau_w$ for $y/\delta < 0.2$ in the present zero-pressure-gradient, incompressible flows, the velocity scale $(\tau/\rho)^{\frac{1}{2}}$ is the same as $U_\tau$.

The spectra in 16 are compared with Bradshaw's (1967*b*) measurements from inner regions of two different self-preserving, equilibrium, boundary layers developing over smooth walls: one with a zero-pressure gradient ($a = 0$) and one with an adverse pressure gradient ($a = -0.255$), where $U_\infty \propto x^a$. According to Bradshaw, his $\overline{u'^2}$ spectra are 'grossly dissimilar for $k_1 y < 2$', and results from the present study fall within the scatter of his measurements. In addition, the normalized fully rough spectra from the present study at $y^+ = 261$ and 485 are the same for $k_1 y > 0.2$, closely following the smooth-wall result measured at $y/\delta = 0.20$ and $a = 0$.

Perry & Abell (1977) present spectra measured in a smooth-walled pipe at $y^+ > 100$ and $y/R < 0.1$ (where $R$ is pipe radius) for Reynolds numbers ranging from $80 \times 10^3$ to $260 \times 10^3$. Using these measurements, these authors showed that broadband results from rough-walled pipe flow obey the same structural similarity laws as smooth-walled pipe flow, provided that both flows have the same large-scale geometry. The extent of Perry & Abell's smooth-walled pipe spectra in $f_u(k_1)/yU_\tau^2$ versus $k_1 y$-coordinates is indicated in figure 16, and shows agreement with the present fully rough results when $k_1 y > 0.1$–$0.2$. In spectra from both flows, regions exist where $f_u(k_1)/U_\tau^2 y$ is proportional to $(k_1 y)^{-1}$, where the smooth-pipe spectra show this over a wider $k_1 y$ range.

The similarity of smooth and fully rough spectra in figure 16 for $k_1 y > 0.1$–$0.2$ is a result of 'active' motions and universal wall structure in inner boundary-layer regions. For $Re_k$ values between smooth and fully rough flow regimes when the flow is transitionally rough, 'active' motion portions of the spectra would be expected to lie on the same curve. Spectral variations at low $k_1 y$ correspond to non-universal, 'inactive' motions.

## 6. Conclusions

The change from smooth to fully rough behaviour in boundary layers over uniform-spheres roughness is more abrupt and occurs over a smaller range of roughness Reynolds numbers than for boundary-layer flows over sandgrain roughness. For mean-velocity and mean-temperature profiles, changes from smooth to fully rough behaviour are described using log-region velocity and temperature-profile shift parameters, $B$ and $B_{\text{th}}$.

The most salient changes in turbulence structure with $Re_k$ were observed in $\overline{u'^2}$ profiles within 23 sandgrain roughness heights from the surface. The changes are believed to be tied to variations in the thickness and character of the viscous sublayer, and changes in the intensity and distribution of the ejection–sweep cycle of events. These, in turn, are related to variations in the energy budget, as well as 'active' and 'inactive' motions. The outer 95–98 % of distributions of $\overline{u'^2}/U_\tau^2$ in rough-wall boundary layers approach invariance with $Re_k$, as $Re_k$ both decreases and increases. The invariant $\overline{u'^2}$ profiles for roughness Reynolds numbers greater than 55 correspond to fully rough behaviour, and the invariant $\overline{u'^2}$ profiles for $Re_k$ values less than 15 approach smooth behaviour. In between, the flows are transitionally rough, and the distributions of $\overline{u'^2}/U_\tau^2$ in the inner 10–20 % change continuously from fully rough behaviour to smooth behaviour as the roughness Reynolds number of the flow changes. Fully rough $\overline{u'^2}/U_\tau^2$ profiles can then be distinguished from transitionally rough profiles, since inner regions of the transitionally rough profiles vary significantly with $Re_k$, whereas fully rough profiles do not.

When normalized using $y/U_\tau^3$, the $-\overline{u'v'}(\partial U/\partial y)$ production term shows a peak near $y^+ = 20$ when $Re_k = 21.0$ and the flow is transitionally rough. This peak decreases

| Designation | Wire type – sensor material | Gold-plated | $l$ (mm) | $d$ (μm) |
|---|---|---|---|---|
| A | Tungsten (platinum-plated) | No | 3.00 | 5.0 |
| B | DISA 55F04-tungsten (platinum-plated) | Yes | 1.25 | 5.0 |
| C | Platinum | No | 0.45 | 2.0 |

TABLE 2. Hot-wire sensing elements

in magnitude with $Re_k$ and disappears as $Re_k$ becomes greater than 55 and the flow is fully rough.

The most universal normalizing parameter for the outer regions of $\overline{u'^2}$ and $\overline{q^2}$ profiles is the friction velocity. In contrast, $\overline{w'^2}$ and $\overline{v'^2}$ profiles at different boundary-layer thicknesses and roughness Reynolds numbers greater than 34 collapse on the same curve when non-dimensionalized using the free-stream velocity. When the roughness Reynolds numbers are less than 34, $\overline{w'^2}/U_\infty$ and $\overline{v'^2}/U_\infty$ versus $y/\delta$ profiles diverge from the $Re_k > 34$ curve to approach smooth-wall behaviour.

Spectra of the longitudinal velocity fluctuations are in agreement with Kolmogorov's first and second hypothesis at high-one-dimensional wavenumbers. Spectra in the inner regions of fully rough boundary layers also have similarity to spectra measured in boundary layers over smooth walls when $k_1 y > 0.2$ and when the results are non-dimensionalized using 'active' motion velocity and length scales $(\tau/\rho)^{\frac{1}{2}}$ and $y$.

All of the data reported herein is available in tabulated format in Ligrani *et al.* (1979), which is available from University Microfilms International, 300 N. Zeeb Road, Ann Arbor, MI 48106, USA.

Professor J. P. Johnston and Professor W. M. Kays are to be thanked for fruitful discussions on the research. Professor Peter Bradshaw and Dr J. F. Morrison provided many useful comments after reading several drafts of the manuscript. Mr D. J. Vitanye wrote the software used to plot data in the three-dimensional format shown in figure 6.

## Appendix: The effect of hot-wire imperfect spatial resolution on measurement of fully rough turbulent boundary layers

An experiment was carried out to determine the effect of hot-wire sensing length on measurement of small-scale turbulence in a fully rough turbulent boundary layer. Measurements were obtained using three sensors, each having a different length, as indicated in table 2 where sensor characteristics are given. Each sensor averages fluctuations from eddy motions along its length, because hot-wire sensors respond to eddies having effective sizes equivalent to the sensor length and larger. Thus, hot-wires have imperfect spatial resolution whenever a sensor length is larger than the smallest lengthscale of energy-containing eddies.

Wires A, B and C were used to measure $\overline{u'^2}$ in a fully rough turbulent boundary layer at $U_\infty = 26.8$ m/s, $\delta_2 = 0.558$ cm, and $Re_k = 63.0$. Each sensor had a length-to-diameter ratio $l/d$ greater than 200 so that reduced response resulting from sensor–support stub conduction did not occur. In figure 17, distributions of $\overline{u'^2}$, measured using these wires, are different in the inner 30–40 % of the boundary layer. At $y'/\delta = 0.078$, the turbulence intensity $\overline{u'^2}$ measured with the 0.45 mm long sensor

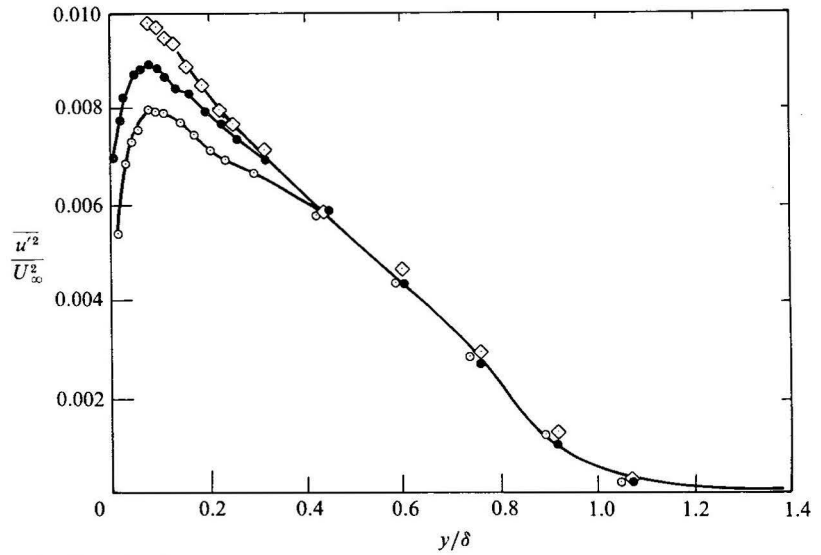


FIGURE 17. Longitudinal turbulence-intensity profiles in a fully rough turbulent boundary layer measured using hot wires with different sensing lengths, $U_\infty = 26.8$ m/s, $\delta_2 = 0.558$ cm, $Re_k = 63.0$; ⊙, sensor A; ◉, sensor B; ◇, sensor C (see table 1).

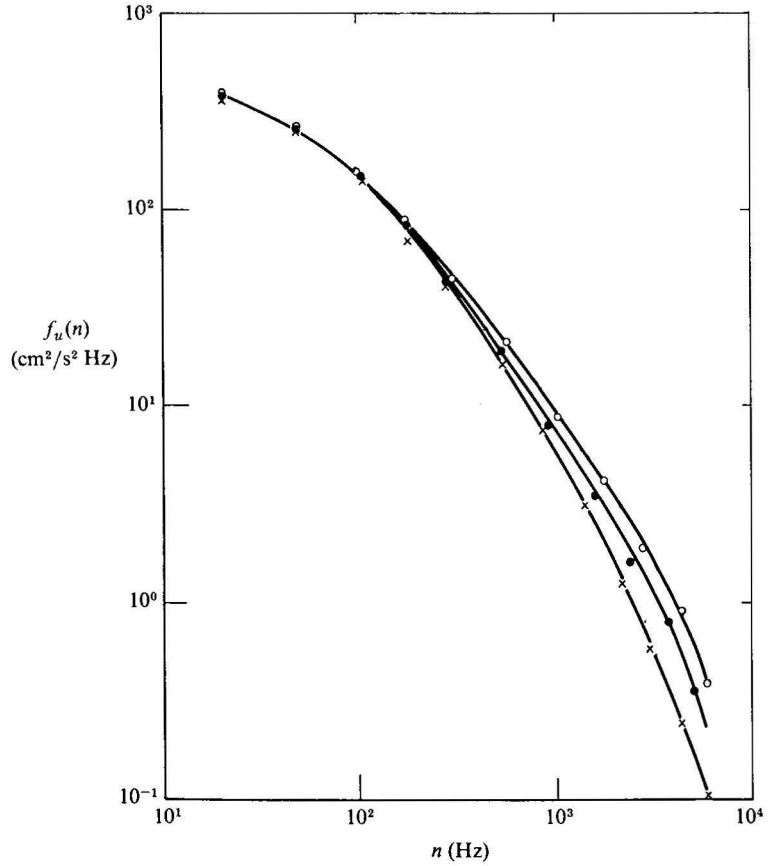


FIGURE 18. Spectra of longitudinal turbulence intensity in a fully rough turbulent boundary layer, $y'/\delta = 0.078$, measured using hot wires with different sensing lengths: ×, sensor A; ●, sensor B; ○, sensor C.

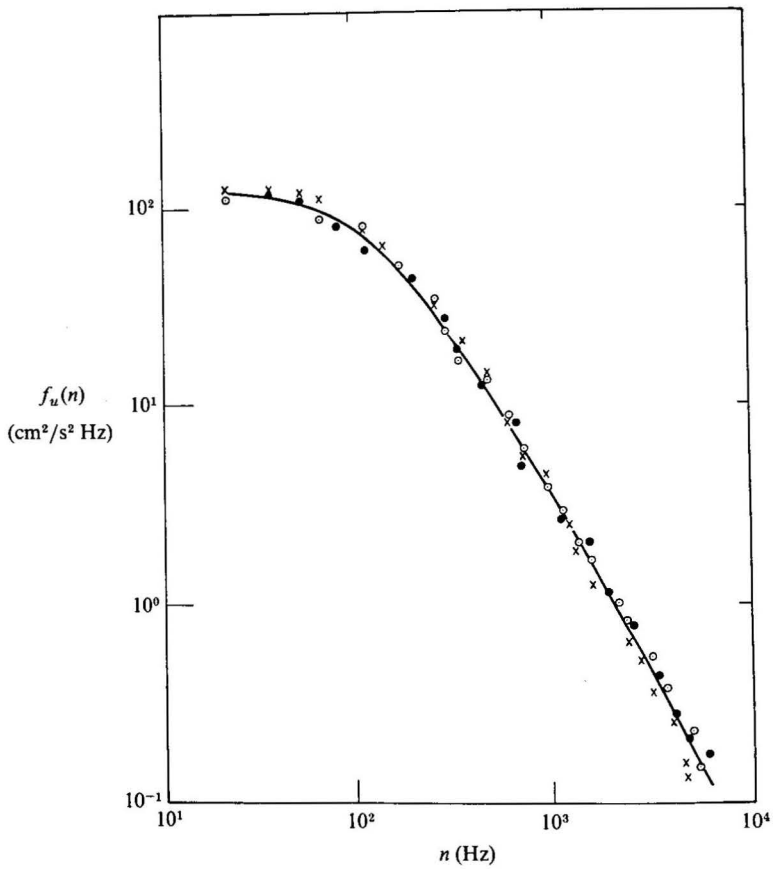


FIGURE 19. Spectra of longitudinal turbulence intensity in a fully rough turbulent boundary layer, $y'/\delta = 0.600$, measured using hot wires with different sensing lengths: same symbols as figure 18.

is as much as 13% greater than that measured with the 1.25 mm long sensor. Similarly, $\overline{u'^2}$ from the 1.25 mm sensor is as much as 12% greater than that measured with a 3.00 mm long sensor. Because each sensor measures motions having length-scales approximately equal to sensor length and larger, the difference between $\overline{u'^2}$ measured with two different length sensors approximates the energy level of motions having scales greater than the shorter sensor and less than the longer sensor. As $y/\delta$ increases in figure 17, magnitudes of $\overline{u'^2}$ measured using sensors A, B and C converge on the same curve. Thus, for $y/\delta > 0.3$–0.4, most longitudinal turbulence energy is due to turbulence motions having spanwise lengthscales greater than 3.00 mm.

At $y'/\delta = 0.078$, the dimensional frequency spectra in figure 18 provide confirmation that $\overline{u'^2}$ differences are a consequence of small-scale structure. In this figure, at lower frequencies, the spectra are the same regardless of wire sensing length; however, when $f > 500$ Hz, the spectra diverge. Resulting differences are significant since they extend to frequencies low enough to be well inside the inertial sub-range. At a given frequency, the highest energy is measured by the smallest sensor.

Spectra at $y'/\delta = 0.600$, shown in figure 19, are different from those presented in figure 18, because spectra are the same regardless of wire-sensing length. This is

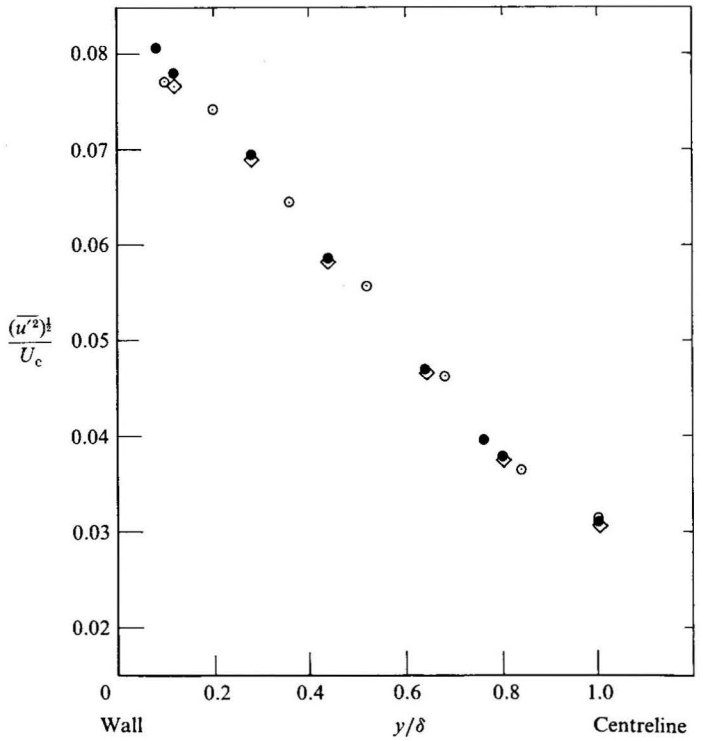


FIGURE 20. Longitudinal turbulence intensity profiles in a smooth-wall channel, Reynolds number based on channel half-width $= 2.94 \times 10^4$, $U_c = 14.2$ m/s: same symbols as figure 17.

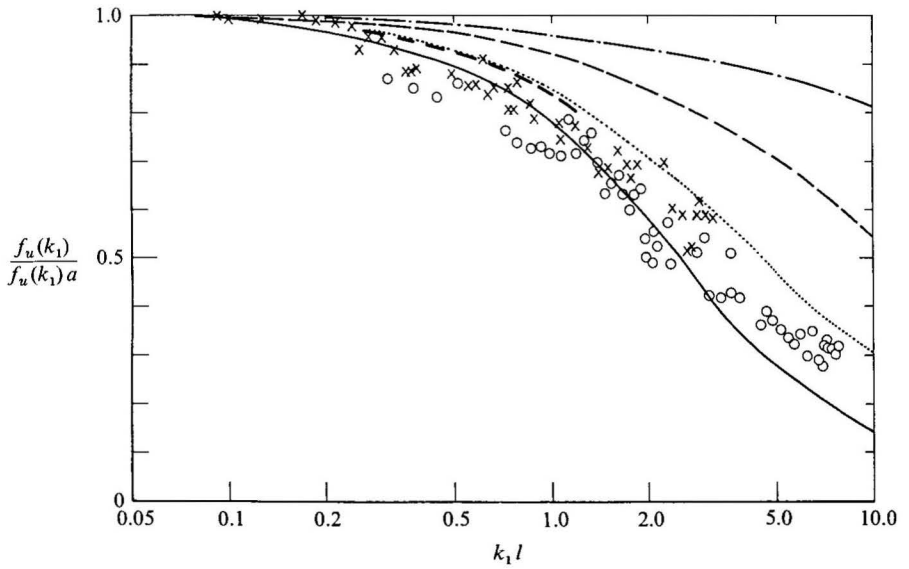


FIGURE 21. Comparison of the Wyngaard (1968) hot-wire-sensor length correction with results from the present study for $\eta = 41$ μm and $y'/\delta = 0.078$: – – –, $l = 450$ μm, $\eta/l = 0.091$ (used to determine $f_u(k_1)\,a$); ×, $l = 1250$ μm, $\eta/l = 0.033$; ○, $l = 3000$ μm, $\eta/l = 0.014$. Wyngaard (1968): —·—, $\eta/l = 1.0$; – – –, $\eta/l = 0.35$; ·····, $\eta/l = 0.10$; ——, $\eta/l = 0$.

expected from figure 17 results and provides a check on spectral measurement procedure.

Additional checks on sensor performance, calibration and measurement procedures were made using a fully developed, smooth-wall channel flow. In the outer 90%, figure 20 shows that hot-wire sensors A, B and C each measured the same $(\overline{u'^2})^{\frac{1}{2}}/U_c$ profile, where centreline velocity $U_c$ equals 14.2 m/s. This further validates measurement procedure, and indicates that the smallest lengthscale of energy-containing eddies is greater than 3.0 mm, even though much-smaller-scale activity would be expected closer to channel surfaces.

The spectra shown in figure 18 are compared in figure 21 with Wyngaard's (1968) correction graph to account for the effect of sensor spatial resolution in isotropic flow. In order to make the comparison, the actual spectrum $f_u(k_1)a$, free of the effect of finite-sensor spatial resolution, was needed. This was computed by correcting the spectrum from the 0.45 mm long sensor using Wyngaard's procedure. The resulting 'true' spectrum was then used to normalize spectra from the 1.25 and 3.00 mm long sensors, and the results were then plotted on Wyngaard coordinates as shown in figure 21. Because the 'true' spectrum at $y'/\delta = 0.078$ agrees with Pao (1965), having an inertial subrange and showing evidence of local isotropy at high wavenumbers ($Re_\lambda = 199$, $\epsilon = 1.19 \times 10^3$ m$^2$/s$^3$), results in figure 21 show good agreement with Wyngaard's correction graph, considering the scatter resulting from any detailed comparison of spectra. Thus, the Wyngaard correction, which is based on Pao's (1965) spectral formulation, is supported by the present measurements.

According to figure 21, the true spectrum and the one measured with the 0.45 mm long sensor ($\eta/l = 0.091$) are 16% different at $k_1 l \sim 1.0$. However, because the Wyngaard (1968) correction applies (in this case) only to the higher-frequency spectrum parts containing only a very small portion of the total energy, magnitudes of $\overline{u'^2}$ in figure 17 from the 0.45 mm sensor at $y'/\delta = 0.078$ ($y^+ = 261$) are 1.1% less than energy levels measured using a sensor having totally adequate spatial resolution. These differences are expected to be larger at smaller $y^+$.

## REFERENCES


Andreopolous, J. & Bradshaw, P. 1981 Measurements of turbulence structure in the boundary layer on a rough surface. *Boundary-Layer Met.* **20**, 201–213.

Antonia, R. A. & Luxton, R. E. 1971 Energy balance in a turbulent boundary layer on a rough wall. *Phys. Fluids* **14**, 1027–1029.

Bradshaw, P. 1967*a* The turbulence structure of equilibrium boundary layers. *J. Fluid Mech.* **29**, 625–645.

Bradshaw, P. 1967*b* 'Inactive' motion and pressure fluctuations in turbulent boundary layers. *J. Fluid Mech.* **30**, 241–258.

Champagne, F. H. 1978 The fine-scale structure of the turbulent velocity field. *J. Fluid Mech.* **86**, 67–108.

Clauser, F. H. 1956 The turbulent boundary layer. In *Advances in Applied Mechanics*, vol. 4, pp. 1–51. Academic Press, New York.

Coleman, H. W., Moffat, R. J. & Kays, W. M. 1977 The accelerated fully rough turbulent boundary layer. *J. Fluid Mech.* **82**, 507–528.

Dipprey, D. F. & Sabersky, R. 1963 Heat and momentum transfer in smooth and rough tubes at various Prandtl numbers. *Intl J. Heat Mass Transfer* **6**, 329–353.

Grass, A. J. 1971 Structural features of turbulent flow over smooth and rough boundaries. *J. Fluid Mech.* **50**, 233–255.

Hama, F. R. 1954 Boundary layer characteristics for smooth and rough surfaces. *Trans. Soc. Nav. Archit. Mar. Engrs* **62**, 333–358.

HEALZER, J. M., MOFFAT, R. J. & KAYS, W. M. 1974 The turbulent boundary layer on a rough, porous plate: Experimental heat transfer with uniform blowing. Report no. HMT-18, Thermosciences Division, Department of Mechanical Engineering, Stanford University.

JOHANSSON, A. V. & ALFREDSSON, P. H. 1983 Effects of imperfect spatial resolution on measurements of wall-bounded turbulent *Bx* shear flows. *J. Fluid Mech.* **137**, 409–421.

JORGENSEN, F. E. 1971 Directional sensitivity of wire and hot-film probes. DISA information no. 11.

KAWALL, J. G., SHOKR, M. & KEFFER, J. F. 1983 A digital technique for the simultaneous measurement of streamwise and lateral velocities in turbulent flows. *J. Fluid Mech.* **133**, 83–112.

KAYS, W. M. & CRAWFORD, M. E. 1980 *Convective Heat and Mass Transfer*, 2nd edn. McGraw-Hill, New York.

LIGRANI, P. M. & MOFFAT, R. J. 1979 Artificially thickening a smooth-wall turbulent boundary layer. *AIAA J.* **17** (8), 907–910.

LIGRANI, P. M. & MOFFAT, R. J. 1985 Thermal boundary layers on a rough surface downstream of steps in wall temperature, *Boundary-Layer Met.* **31** (2), 127–147.

LIGRANI, P. M., MOFFAT, R. J. & KAYS, W. M. (August) 1979 The thermal and hydrodynamic behaviour of thick, rough-wall, turbulent boundary layers. Report no. HMT-29, Thermosciences Division, Department of Mechanical Engineering, Stanford University.

LIGRANI, P. M., MOFFAT, R. J. & KAYS, W. M. (June) 1983 Artificially thickened turbulent boundary layers for studying heat transfer and skin friction on rough surfaces. *Trans. ASME* I: *J. Fluids Engng* **105** (2), 146–153.

LIU, C. K., KLINE, S. J. & JOHNSTON, J. P. 1966 An experimental study of turbulent boundary layers on rough walls. Report no. MD-15, Thermosciences division, Department of Mechanical Engineering, Stanford University.

MONIN, A. S. & YAGLOM, A. M. 1971 *Statistical Fluid Mechanics*, vol. 1. The MIT Press.

NIKURADSE, J. 1933 Strömungsgesetze in rauhen Röhren. VDI Forschungsheft, no. 361. 1950, English Translation, NACA-TM 1292.

ORLANDO, A. F., MOFFAT, R. J. & KAYS, W. M. (May) 1974 Turbulent transport of heat and momentum in a boundary layer subject to deceleration suction and variable wall temperature. Report no. HMT-17, Thermosciences Division, Department of Mechanical Engineering, Stanford University.

OWEN, P. R. & THOMSON, W. R. 1963 Heat transfer across rough surfaces, *J. Fluid Mech.* **15**, 321–334.

PAO, Y. H. (June) 1965 Structure of turbulent velocity and scalar fields at large wavenumbers. *Phys. Fluids* **8** (6), 1063–1075.

PERRY, A. E. & ABELL, C. J. 1977 Asymptotic similarity of turbulence structures in smooth- and rough-walled pipes. *J. Fluid Mech.* **79**, 785–799.

PERRY, A. E., SCHOFIELD, W. H. & JOUBERT, P. N. 1969 Rough wall turbulent boundary layers. *J. Fluid Mech.* **37**, 383–413.

PIMENTA, M. M., MOFFAT, R. J. & KAYS, W. M. 1975 The turbulent boundary layer: an experimental study of the transport of momentum and heat with the effect of roughness. Report no. HMT-21, Thermosciences Division, Department of Mechanical Engineering, Stanford University.

ROTTA, J. C. 1962 Turbulent boundary layers in incompressible flow. *Prog. Aerospace Sci.* **2**, 1–219.

SABOT, J., SALEH, I. & COMTE-BELLOT, G. 1977 Effects of roughness on the intermittent maintenance of Reynolds shear stress in pipe flow. *Phys. Fluids* **20** (10), part 2, S150–S155.

SCHETZ, J. A. & NERNEY, B. 1977 Turbulent boundary layer with injection and surface roughness. *AIAA J.* **15** (9), 1288–1294.

SCHLICHTING, H. 1968 *Boundary-Layer Theory*, 6th edn. McGraw-Hill.

TOWNSEND, A. A. 1954 *The Structure of Turbulent Shear Flow*, 1st edn. Cambridge University Press.

TOWNSEND, A. A. 1976 *The Structure of Turbulent Shear Flow*, 2nd edn, pp. 150–158. Cambridge University Press.

TUTU, N. K. & CHEVRAY, R. 1975 Cross-wire anemometry in high intensity turbulence. *J. Fluid Mech.* **71**, 785–800.

WILLMARTH, W. W. & SHARMA, L. K. 1984 Study of turbulent structure with hot wires smaller than the viscous length. *J. Fluid Mech.* **142**, 121–149.

WOOD, D. H. & ANTONIA, R. A. 1975 Measurements in a turbulent boundary over a D-type surface roughness. *Trans. ASME* E: *J. Appl. Mech.* **42**, 591.

WYNGAARD, J. C. 1968 Measurement of small-scale turbulence structure with hot wires. *J. Phys.* E: *Sci. Instrum.* **1**, ser. 2, 1105–1108.